Radar Horizon Estimation from Monoscopic Shadow Photogrammetry of Radar Structures:
A Case Study in the South China Sea

by

James E. Luttrull

A Thesis Presented to the
Faculty of the USC Graduate School
University of Southern California
In Partial Fulfillment of the
Requirements for the Degree
Master of Science
Geographic Information Science and Technology

May 2018

Quaesita Marte Tuenda Arte

Table of Contents

List of Figures

List of Tables

Acknowledgements

My studies in Geospatial Science began through conversation with Dr. Darren Ruddell, who encouraged my nascent interest in geography and opened my eyes to the world of data science. Dr. Steven Lamy highlighted the importance of Geospatial Science as a complement to my study of International Relations and provided guidance and opportunities for this technical skill to flourish in my native field. Dr. Steven Fleming in turn prompted my decision to begin a Master's program in Geospatial Information Science & Technology, and provided invaluable mentorship throughout my studies, research, and career development. Work with Armament Research Services cultivated a spirit and tradecraft of adventurous, complex problem solving. These mentors have shaped my academic success throughout university and post-graduate life.

Dr. Steven Fleming's guidance as advisor to this thesis was additionally invaluable, as was that of committee members Dr. John Wilson and Dr. Andrew Marx. It did not hurt to have the advice and awareness of two veterans of the United States Army and United States Air Force officers in Dr. Fleming and Dr. Marx, graduates of their respective service academies to boot. Dr. John Wilson's wealth of knowledge, both of world geographic features as well as geospatial technologies was instrumental in many minor details throughout. Thanks is also due to Dr. Andrew Coe, whose courses inspired this research topic.

This project attempts to increase the accuracy of published data and reportings of the Center for Strategic & International Studies, and so great appreciation must be shown to their prompt email responses and help in locating mutual data sources to aid in an accurate analysis. The DigitalGlobe Foundation is likewise acknowledged for their generous, timely, and cost-free imagery provision.

Abbreviations and Terminology

A2AD   Anti-Access & Area Denial

ADIZ   Air Defense Identification Zone

AMTI   Asian Maritime Transparency Initiative

China   People's Republic of China (PRC)

CSIS   Center for Strategic & International Studies

DEM   Digital Elevation Model

GIS   Geographic Information System

HF   High Frequency

LOS   Line-of-Sight

NDL   Nine-Dash Line

OTH   Over-the-Horizon

PRC   People's Republic of China ("mainland China")

RS   Remote Sensing

SCS   South China Sea

SSI   Spatial Sciences Institute

Taiwan   Republic of China

USC   University of Southern California

Abstract

The People's Republic of China's (PRC) militarization of artificial islands in the South China Sea (SCS) represents a challenge to security of, and freedom of navigation in, international waters. Static defenses on these islands enhance Anti-Access and Area Denial (A2AD) efforts, allowing de facto sovereignty in the area sustained by successful radar coverage. While many A2AD tools may not be measured without direct access to the product, conventional radar structure heights may be measured remotely, allowing for indirect measurement of an adversary's radar range. Though estimates for these ranges have been published by various defense thinktanks, this study builds on shadow analysis literature to perform more accurate measurement and projection of radar ranges through use of remote sensing and trigonometry applied to imagery of SCS radar construction in late 2017.

This study uses shadow analysis to measure radar tower heights combined with radio wave propagation equations to provide a viable alternative to rule-of-thumb estimation. This novel methodology is tested on radar arrays identified by the Center for Strategic and International Studies (CSIS) on three key islands in the SCS's Spratly Islands. Radar horizon range measurements provide a detailed analysis of radar coverage at various altitudes, showing that previously published estimates can differ from bespoke analysis by more than double. The study quantifies average range of radar arrays on artificial islands created by the PRC, finding the average radar to reach radar horizon in 23.82 km distance at 0 m altitude; equal to 249.47 km at 3,000 m, or 435.81 km at 10,000 m, respectively.

Chapter 1 Introduction

This study combines traditional Remote Sensing (RS) imagery analysis with Geographic Information Systems (GIS) to measure the radar horizons of a select group of radar structures identified by the Center for Strategic and International Studies (CSIS) and their Asian Maritime Transparency Initiative (AMTI). The radar structures, or radar towers, are located on artificial islands and reclaimed land in the South China Sea (SCS) by the People's Republic of China (China) in the 2010s.

Radar serves a vital role in China's territorial defense and Anti-Access (A2) and Area Denial (AD) tactics currently of concern to strategic thinkers. The radio waves used by radar are nonetheless limited by line-of-sight (LOS) and, therefore, radar vision is limited by positioning. The placement – and especially heights – of radar systems has a powerful effect on LOS and is vital to measuring radar range. Assessing these positions and heights is difficult as a function of their military classification and the limited publishing of defense information on system capabilities. The CSIS and AMTI have previously identified radar ranges for these towers using common industry estimates. This study tests a method for more accurate estimation of radar ranges, as necessary for analysis of the PRC's A2AD capabilities, strengths, and weaknesses in the SCS.

1.1. Motivation

This project parallels the recent changes in the SCS, the geostrategic effects of militarization of new Chinese islands, and the increased accessibility of RS to the public as an open source analysis community. Chinese territorial claims, outlined by the Nine-Dash Line (NDL) have taken an adversarial nature against rival claims with various other Southeast Asian states. Reinforcing Chinese claims, various artificial islands have been built of reclaimed land on

1

the existing sites of reefs and atolls, complete with military infrastructure. With commercial and open source satellite imagery available at limited or no cost, a new age of imagery analysis by private citizens has come to rival commercial and government intelligence outfits.

To this end, there is opportunity to enhance public reporting by the think tanks such as the Center for Strategic and International Studies' Asian Maritime Transparency Initiative (AMTI). While most of the military tools discussed by CSIS/AMTI are out of reach under the supervision of a foreign military, radar structure heights, and, therefore, ranges, are available for measurement via readily accessible RS imagery. Radar is the first line of A2AD defense, and understanding its range is vital for informing the public about an adversary's true military capabilities. Therefore, the proposed study takes a novel approach that combines open source GIS and RS methods and data to solve a relatively overlooked problem that experts project to be at the core of future US military confrontation.

1.2. Research Objective

This thesis examines the radar coverages of China's new radar stations built in the South China Sea, and reviews the coverage compared to other known weapon systems and to radar coverage estimates from CSIS/AMTI publishing. This project measures radar tower heights via shadow analysis; uses these height measurements to measure radar horizons from each tower at various altitudes; compares these coverages with weapon system ranges previously identified on the islands to search for strengths and weaknesses in coverage overlap; and, finally, compares these ranges to CSIS/AMTI data, to evaluate the discrepancy between the study's calculations and estimates.

1.3. Scope & Data

This project focuses on a limited – but key – portion of published estimates by CSIS/AMTI. The study addresses these estimates in reference to identified radar structures on newly dredged Chinese islands in the Paracel and Spratly island chains, shown in Figure 1. To increase the accuracy of published estimates, this study calculates radar ranges for structures on the "Big Three" islands in the Spratly chain which CSIS/AMTI has confirmed have new radar stations: Mischief Reef, Fiery Cross Reef, and Subi Reef (AMTI).
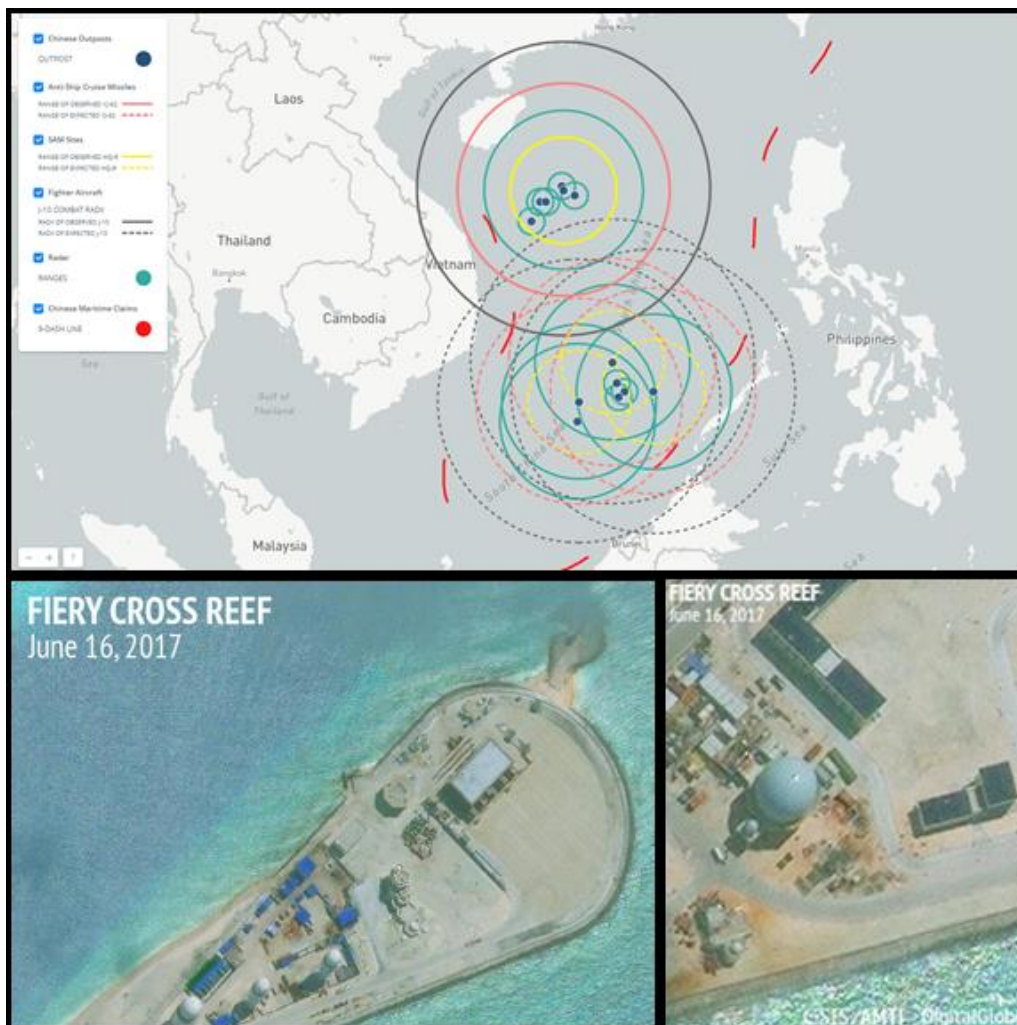
Figure 1: GIS and RS Publishings of Ranges and Radar Tower Identification. Source: AMTI 2017

While this study proposes a method applicable to any potential radar tower visible in aerial or satellite imagery, the focus of this project is tailored to a selection of militarized artificial islands in the SCS occupied by China. Out of seven of these features in the furthest island chain, the Spratlys, three are distinguished by a substantially larger reclaimed area, level of infrastructure, and military activity. These "Big Three" are comprised of Mischief Reef in the north of the Spratlys, Fiery Cross Reef to the west, and Subi Reef to the east. They form a triangle around all but one of the other seven islands (Johnson Reef South, Hughes Reef, and Gavens Reef inside, with Cuarteron Reef outside). According to CSIS/AMTI and other researchers cited throughout this work, the "Big Three" form the core of a potential PRC military launch pad while providing defensive coverage for interior islands. The only island in the chain outside the "Big Three" triangle is Cuarteron Reef, where numerous radar arrays allegedly make this a forward reconnaissance base (Lee 2015). Imagery from CSIS of these artificial islands is provided below in Figures 2 - 4.
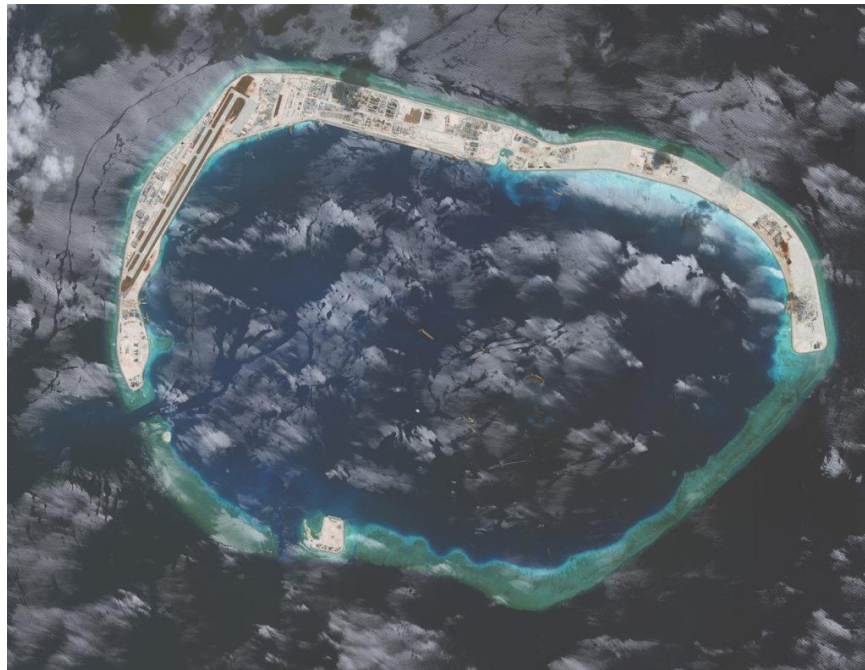
Figure 2: Mischief Reef, July 2016. Source: CSIS Island Tracker.

Figure 3: Fiery Cross Reef, June 2016. Source: CSIS Island Tracker.

Figure 4: Subi Reef, July 2016. Source: CSIS Island Tracker.

1.3.1. Data

Analysis for this study has been provided by CSIS, including data of digitized points based on imagery provided by GeoEye, publicly available for academic study and published to ArcGIS Online, as well as to the CSIS website in .kmz format, though of poor quality. Imagery for this analysis was provided by the DigitalGlobe Foundation, without which this study could not be performed.

Chapter 2 Background and Literature Review

PRC island building in the SCS is an attempt to create de facto sovereignty in the region using longstanding but unrecognized territorial claims. Control over the SCS can provide the PRC assured access to the resources held within its boundaries, give buffer against forces invading the homeland, and open routes of communication, trade, and surveillance. Territorial claims like China's often follow historic precedent or cite historic need, while tactics for control over territory adapt to a given state's current technology and potential adversaries. The modern tool of radar finds itself as a prime facilitator of territorial defense, especially considering recent shifts toward modern asymmetric defense strategies, including A2AD. Radar relies greatly on LOS vision for the transmission and reception of radio signal, and therefore is constrained by physical geometry and the curvature of the Earth. Identification of radar infrastructure is a necessary pursuit of counter-A2AD strategy and relies greatly upon RS tactics. Gaps remain in the RS evaluation of radar heights to measure radar LOS range.

This chapter first describes the history of the region and China's relationship with the territory in question. This is followed by a discussion of claimants and the contest of territorial rights to the SCS. The nature of A2AD is then discussed within the context of the SCS. Radar as a tool of A2AD is examined. Review of existing RS and GIS radar analyses completes the chapter, to highlight the research already existing within the field.

2.1. The South China Sea in History and International Relations

As the issue of territorial claims in the SCS is fundamentally a concern of international relations, viewing it through a social science lens can offer great clarity to the root of the problem. In this light, the SCS is much like other bodies of water bordered by multiple states. It is a shared space, but this space can be used for cooperation or competition. The SCS's

geopolitical role as an international space has therefore been analyzed in comparison to the politics of other shared seas, with a range of resulting models. The US-Caribbean model represents a system of disinterested hegemony (Kaplan 2014), whereby China casually controls and maintains the politics of the region through indirect means. The Germany-North Sea model focuses on the nature of limited sea-lane access through the body in wartime (O'Mara 2013), and highlights China's concern for access to the SCS, leading to a more confrontational and risk-tolerant attitude in the region. The Europe-Mediterranean model supposes a region of economic competition despite shared culture (Evers 2013) and assumes that international consensus can be reached for mutual maintenance and access in the SCS. While the prevailing literature cited in this section and Section 2.2 take a tone more reminiscent of the first two models, there is hope that a more cooperative outcome is possible. All these theories, however, pivot around economic objectives and security concerns based on historical precedent. PRC development of artificial islands in the SCS is therefore integrally related to the exploitation and defense of the territory.

2.1.1. Access to Trade & Resources

Chinese contact, and trade, with the remainder of the world has traditionally flowed through the SCS. China has long "perceived themselves dominant" over the sea lanes that ran south through the Strait of Malacca, despite distance and the development of modern rivals in the region (Souza 2014). Chinese trading through the SCS dates from 500 BCE (Gungwu 1954) and was maintained as what "may well be the most enduring maritime trade route in history" despite intermittent closure during wartime (Gao & Jia 2013). A great manner of wealth has consistently traveled between civilizations along this route, where "the Chinese exchanged their silks and other manufactured goods for luxury goods like ivory, pearls, tortoise shells, kingfisher and peacock feathers, rhinoceros horns and cinnamon and scented woods" in preindustrial eras, to

oil, steel, and manufactured goods today (Gangwu 1954). In 2016, $3.37 trillion – or 21% of all global trade – moved through the SCS (China Power Team 2017).

The SCS contains a variety of natural resources for extraction as well. Mid-range estimates put the amount of petroleum beneath the seabed at 11 billion barrels, with 190 trillion cubic feet of natural gas (EIA 2013). While some of these reserves are outside disputed territory, an enormous flow of traded energy resources still travels through the SCS by ship as well. These petroleum and natural gas products onboard tanker ships passing through the SCS are of immense value, regardless of what lies below the sea they travel on.

Additionally, undersea telecommunication cables, including the fiberoptic cables that anchor the global Internet, pass in high density through the SCS. These cables have recently come to the fore of international security discussions due to their vulnerability and structural importance to global trade and communication (Tsuruoka, 2018).

2.1.2. SCS as Path of Invasion

While resource access regards economic concerns, many attempt to understand the SCS through its history as a conflict zone. Before the colonial and modern eras, China consistently maintained control of the SCS and exerted power into the broader world through it. However, after the Portuguese conquest of Malacca in 1511, Western powers reversed the flow of East-West power dynamics and "disturbed China's world order" (Souza 2004). For the past two centuries, "the South China Sea has been an avenue of approach for Westerners who invade China. There is a historic baggage associated with the vulnerability of the South China Sea." (McDevitt 2016). As the PRC's international power and presence grows – or returns – there is historical precedent that China will attempt to control the SCS again.

2.2. South China Sea Border Claims

The importance of the SCS is evident through the contest of claims over it. China's claim in the SCS does not exist in a vacuum, as Vietnam, the Philippines, Malaysia, Taiwan, and Brunei share both legitimized and dubious claims to the area as well. These claims have been summarized in Figure 5 below by the Wall Street Journal (Page 2016).
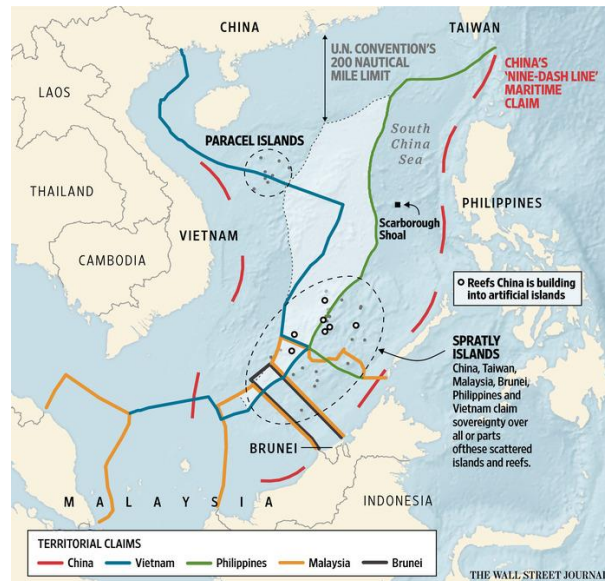
Figure 5: Competing Claims for the SCS. Source: Wall Street Journal, 2016

2.2.1. China's Claim

Today, the PRC's SCS island building has been correlated with heightened reference to the Nine-Dash Line territorial claim. The Nine-Dash Line (NDL) claim originates from 1930 (Li & Li 2003) as a solid, not dashed, "U-Shaped Line" to standardize maps made in the nation. This solid boundary showed Chinese territorial control over much of the SCS, far beyond the standard 200 nmi boundary permitted by the future United Nations' Convention on the Law of the Seas (UNCLOS). Nonetheless, the first dashed line was published later without international dissent or comment, with an eleven-dashed line released over 1947 and 1948 (see Figure 6). The eleven-dashed line was later reduced to nine dashes, to reduce infringement on Vietnam's maritime

claim, and become the modern NDL (Brown 2009). Today, a frequently-referenced tenth line exists to the east of the Republic of China (Taiwan); however, this line is less disputed and politically separate from the SCS conflict.

Based on the summative historic precedent of their claims in the SCS, China has maintained that they hold sovereignty in the area. Despite this, the PRC has infrequently exercised this power until the 2010s, when the NDL became a topic of contention to many states throughout the Pacific Rim (see Figures 5 & 6). This is largely because the modern NDL overlaps with territorial claims of Vietnam, Malaysia, Brunei, and the Philippines. Most of these nations' claims equally overstep the UNCLOS 200 nautical mile limit, although by a much lesser distance and over vastly smaller areas.
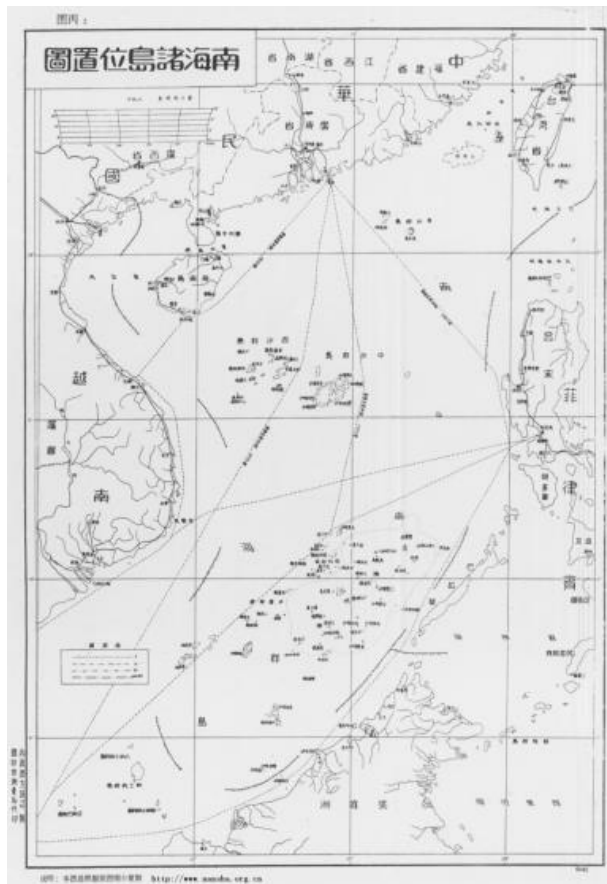
Figure 6: Original 1940s "U-Shaped Line" with 11 Dashes. Source: Hayton; The Diplomat

Despite the NDL territorial claims, China has elaborated very little on the legitimacy of its sovereignty over the area. This elaboration is necessary to ground the claim in legitimate international law. One source of potential legitimacy commonly referenced is historical precedent of the territorial claim. Li & Li (2003) outline that China has nearly fulfilled the requirements to claim "historic waters" as outlined by the International Law Committee by the United Nations Secretariat in 1962, but has stopped short of the processing this claim through any international body. Like all other potential methods of acquiring claim legitimacy, the "historical waters" claim has nonetheless not been officially stated for international review. Much like the purposeful vagueness of the NDL, whose dashes leave cartographers in confusion, China has made "no official claims other than a claim to 'sovereignty' [in the SCS]… No spokesman has ever gotten up and said, 'the official position of the government of China is X.'" This hamstrings the international community from resisting the PRC's SCS takeover, as the PRC has not "even [published] a credible maritime entitlement claim that [one] could protest as excessive" (McDevitt 2016). Overall, this fails to define sovereignty, territorial control, and legitimacy in the SCS. The situation is therefore ripe for land grabs and de facto annexation.

2.2.2. Other Claimants

Other regional claimants have strong interests – both for and against – the enforcement China's NDL. Taiwan backs China's NDL due to similar land claims on Taiping Island and has supported China's claims in international court (see PDCC 2015). Considering historic "acquiescence" to China's claim by neighbors (Zhao 1999), the government of Taiwan considers "the entire area within the U-shaped line to be China's historical waters" (Cheng-yi 1997). Taiwan even often references the original phrasing – "U-shaped line" – rather than the newly termed "Nine-Dash Line" (Wang 2010).

In 2013, a legal battle initiated by the Philippines became a topic of concern for SCS claimants and neighbors. In the case, international courts sought to establish a precedent based on UNCLOS jurisdiction over the SCS. In 2016, the Philippine plaintiffs won the case, but many supporters remained disappointed with the outcome. Jurists have complained that no real result was reached despite the Philippine victory, as Chinese economic pressure effectively nullified any enforcement of the decision, leading the Philippines to pull back from the territory rather than exert their legitimate claim (Sofaer 2016).

Vietnam has faced a similar situation in previous decades, but with more violent results. Vietnamese claims to the SCS were dampened in 1974 with China's forcible removal of Vietnamese forces from the Paracels, and again in 1988 as the Chinese "sank three Vietnamese supply ships, killed seventy-two Vietnamese, and captured nine" in the Spratlys (Gallagher 1994, 174). Despite this, Vietnam has maintained quiet opposition to Chinese encroachment, encouraged by the US and others to express that, "even though there is not [military] parity, the message gets across to Beijing that their changes to the status quo [in the SCS] are going to be met with other changes that are against their interest" (Cooper 2016). Vietnam has thus found itself allying with PRC-opposing nations on the issue.

In sum, these claims have been specifically identified in relation to natural resource locations, as shown in Figure 7.

Claims on the South China Sea
Six Southeast Asian nations and China contest all or parts of the Spratlys and Paracel islands in the South China Sea

Sources: U.S. Energy Information Administration, U.S. Department of State, Middlebury College, National Geographic
Staff, 28/01/2014
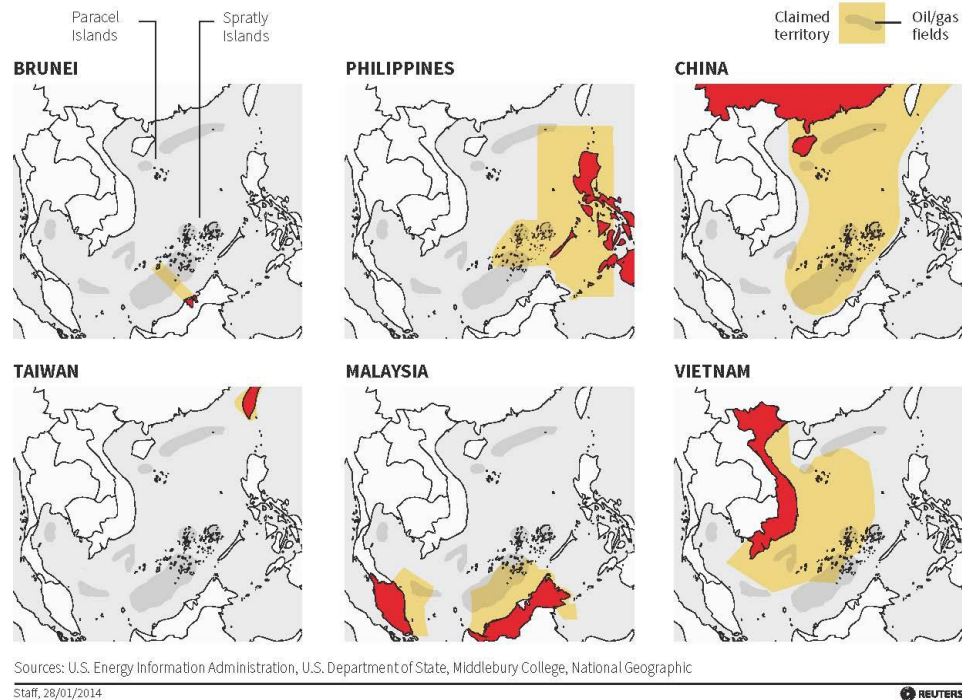
Figure 7: Competing Claims and Natural Resources. Source: The Brookings Institute; Reuters.

2.3. Anti-Access & Area Denial

If PRC island-building fits the explanation of a territorial control attempt within its NDL, the strategy of control and defense of the claim is the next concern. Experts largely agree that the threat posed by Chinese military buildup in the SCS is that of an Anti-Access, Area Denial (A2AD) strategy. A2AD is a topic of increasing research in recent years, as described in this section. To this end, this study draws its relevance from the importance of understanding and countering the described A2AD strategy, and how geospatial techniques may be used for this purpose.

First, there is contention with use of the popular phrase A2AD. The concept of A2AD is not new, nor are the tactics currently used for A2AD a "change [in] the nature of modern warfare" (Davin 2013, 5). The only unique aspect of A2AD is current technological trends

applied to age-old asymmetric tactics of threatening supply and communication routes and making opposing intervention risky. Nonetheless, "the use of the A2AD framework is a critical tool for looking at the operational problem posed by China's military buildup because the US must [assure] allies that it will maintain access" to sea lanes and trade routes (Davin 2013). To acknowledge this fact, this thesis will therefore use the term A2AD to describe defensive asymmetric tactics currently employed by China, for the sake of clarity with existing literature.

The most comprehensive explanation of A2AD toolsets, strategies, and their countermeasures was compiled by Krepinevich (2003) in a manuscript delivered to Congress. The work references changing military tactics as the US entered a new phase of warfare in the 21st Century, detailing the asymmetric tactics of US enemies brought about following the overwhelming US victory in Iraq in 1991. As this trend has continued even up through the current day, the tactics have become more defined, and taken a more deliberately geopolitical focus. As A2AD centers on the control of geographic territory and the placement of defenses within it, the strategy is inevitably built on geospatial units, available for geospatial measurement and analysis: the areas of territory defended, the zones of coverage provided by A2AD systems, and the distances between defenses both static and mobile. A2AD's geopolitical nature therefore avails itself of a GIS frame of investigation.

The need for GIS analysis of A2AD capabilities is evident in the social science realm's growing concern for it over the decades after Krepinevich's (2003) publication. McCarthy (2010) expanded upon Krepinevich's developments nearly a decade on, after the second invasion of Iraq in 2003. He noted an increase in A2AD tactics in the mainstream of anti-US states, confirming Krepinevich's (2003) observation that a new wave of A2AD tactics were on the rise throughout countries traditionally opposed to the US and the West. The current US perspective

on A2AD is additionally outlined by in periodical publications rather frequently. Cheng (2014) discusses the specifics of Chinese interests and US policy objectives against them. Military historians likewise relate Chinese A2AD efforts in the SCS to German attempts at North Sea domination in the Battle for Britain (O'Mara 2013) and underscore the Chinese strategic emphasis on airspace control as a source of A2AD.

The effects of A2AD defenses have powerful strategic and geopolitical effects, with some researchers even encouraging US planners to "abandon or lessen reliance [on attempts at] Air Superiority over Mainland China" due to the high cost of penetrating Chinese air defense structures – radar foremost among them (Overcash 2010). This advice comes with geographic reference, but little geospatial clarity, however. Especially on the issue of radar, the GIS analysis dearth has been highlighted as published discussion of PRC radar capabilities focus on smaller and smaller geographic scales, without touching on measurable specifics. For example, testimony before Congress has detailed the Chinese need for radar extension into the SCS to improve China's "ground-based radars [that] provide overlapping coverage of coastal areas" (O'Rourke 2017; Overcash 2010), but offered little calculable evidence. The literature generally agrees that Chinese A2AD is focused on air power and anti-ship efforts, but almost all A2AD tools can be visualized or measured in a geospatial context. Whatever the A2AD tool of focus, mounting a defense relies on "the first step… the detection of a potential target" via radar systems (Davin 2013). This highlights the importance of radar as a force multiplier, and the great danger it poses to the PRC's potential adversaries. According to Admiral Mike McDevitt, USN (Ret.), "China [is] now, potentially for the first time, achieving defense and depth" in the SCS. Anti-ship and anti-air surveillance "will give them an opportunity to monitor [threats] throughout the SCS. If you chose to use the SCS as an avenue of approach, it would be an interesting go"

(2016). But what avenues are and are not available is far too important a question for regional generalization. A geospatial analysis is needed of A2AD tools, or at least a model of how such calculations might be performed.

Overall, US interests require that it resists Chinese A2AD efforts (Davin 2013; Hoyler 2013; Cheng 2014; McCarthy 2010; Gerson 2011). The most cost-effective method of inhibiting Chinese A2AD is to eliminate the first step in their anti-ship and anti-air "kill chain": ground-based radar surveillance and targeting systems (Davin 2013; Overcash 2010). To do so will require a thorough understanding of the problem that is only available through investigation with a GIS framework, and with an informed understanding of radar itself.

2.4. Radio Propagation and Radar Line of Sight

Radar operates through transmitting radio waves across an area, which reflect off objects and return to a receiver. The receiver then calculates the location, size, and potential movement of the reflecting object based on the returned signal (Skolnik 2007). In many aspects, these radio waves operate much like visible light, and are limited in similar ways to line-of-sight vision. As the Earth is not flat, the curvature of the Earth bends away from a viewer and removes it from line-of-sight, which changes dependent on one's height (Haslett 2008). Beyond the horizon, electromagnetic waves struggle to pass through the dense bulge of the Earth's sphere and are rendered invisible. Simply put, "distance to the horizon depends on your height," and the taller the viewer, the further they can see. In terms of radar, the taller the radar structure, the further away it can observe.

2.4.1. Radar Height as Measure of Range

Height therefore is the dominant factor in establishing visible range for both visible light and radio waves. Via the Pythagorean Theorem, the theoretic distance to the visible horizon is

seen in Equation 1 and illustrated by Figure 8 (for a full catalogue of equations used in this study, see Appendix D).

$$D_h \approx \sqrt{2 \cdot R \cdot H} \qquad (1)$$
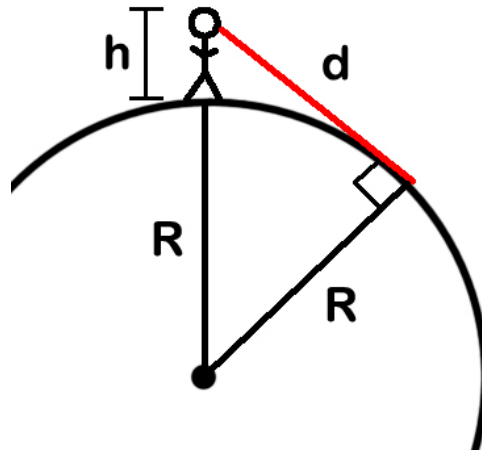
Figure 8: Visual Depiction of Horizon Trigonometry. Source: Plait 2009

where D_h is the distance to the visible horizon, R is the radius of the earth, and H is the height of the viewpoint from the surface of the earth. This equation can be simplified to Equation 2, when using an average radius of the Earth to account for slight variation in its curvature at 6371 km:

$$D_h \approx 3.57 \cdot \sqrt{H} \qquad (2)$$

where D_h is measured in kilometers, and H is measured in meters (NAVAIR 2013, Chp 4; Haslett 2008, 33; Valtr & Pechac 2005, 491). These equations refer to the exact lines-of-sight one might have with human vision. However, various factors affect electromagnetic waves in the radio spectrum differently than the visible light spectrum. In fact, atmospheric conditions and the ability of radio waves to bounce constructively create a "geoclimatic factor," K, that increases radio wave range with a multiplier of 1.33, or four-thirds (Bacon, 271; Haslett 2008). Valtr & Pechac (2005) and other researchers have examined changes in K at various altitudes and

18

environmental conditions. The effect of *K* increases the range of radio waves beyond the horizon, creating a bend for radio waves that is "very slight, but… in the same sense as the curvature of the Earth… [t]he overall result is that the radio horizon is further than the visible horizon" (Haslett 2008). Thus, Equation 2 can be adjusted to Equation 3 as follows to account for *K* when measuring with radio waves:

$$D_h \approx 4.12 \cdot \sqrt{H} \qquad (3)$$

All of these equations, however, only measure a radio line-of-sight maximum, or radar horizon, at the surface of the Earth. To calculate the maximum distance line-of-sight to an object of non-zero height, Equation 4 is used (NAVAIR 2013):

$$D_{max} \approx 4.12 \cdot \left(\sqrt{H_{Origin}} + \sqrt{H_{Target}} \right) \qquad (4)$$

This equation will be used to measure radar ranges based on radar height data, as discussed later. It should equally be noted that Equation 4 may be solved for the unknown height of a given visible object at known distance, using Equation 5 as follows.

$$H_{Unknown} \approx \left(\frac{D_{max}}{4.12} - \sqrt{H_{Known}} \right)^2 \qquad (5)$$

As the equation is not a direct geometric measurement but rather a mathematical approximation, the units used in Equation 4 are still valid.

2.4.2. Radar Beyond Line of Sight

Radio signals can also be bounced off the ionosphere in the upper atmosphere and reflected back down to Earth beyond the traditional LOS-method of conventional radar. This technique, known as Over-The-Horizon (OTH) or High Frequency (HF) radar, is "quite attractive for the radar observation of areas (such as the [surface of the] ocean) not practical with

conventional microwave radar" (Skolnik 2007). Although OTH/HF radar can surveil at ranges up to 2000 nmi, it requires large arrays for both transmitters and receivers which are strikingly different in construction and easily identifiable in aerial imagery. These are standardly constructed either as large "elephant cage" ring structures, or in rowed pickets of small antennae rather than the clear domed towers of conventional ground-based radar structures. Additionally, OTH/HF radar is considered to have a lower resolution and is not always suitable for identifying aircraft or for the detailed targeting of surface vessels (Nathanson 1991, 19). OTH/HF radar additionally has distant minimum ranges. Other forms of extending radar range like the OTH/HF method have been researched for some time, focusing on environments that might affect the coefficient *K*, such as weather or other atmospherics (Booker 1946; Rogers 1957). In terms of the SCS, there is a speculation of a possible OTH/HF "elephant cage" systems on various islands, first identified on Cuarteron Reef (AMTI). This study will focus on traditional conventional radar tower systems nonetheless due to the impracticality of estimating OTH/HF radar without direct access to the system. As it does not follow clear rules for use, like conventional radar's reliance on LOS, it is much more difficult to estimate or calculate remotely.

2.5. Monoscopic Photogrammetry for Shadow Analysis

The range of radar is dependent on the sensor's height, as discussed above. An object's height may be measured using its shadow length, based on geometry of the Sun's angle and the object's location on Earth – a geospatial approach. Because aerial and orbital imagery acquired through remote sensing techniques rarely capture sidelong views of buildings, "an obvious starting point for height estimation is the sun shadow" (Wegner et al. 2014). While this estimation can be performed more easily with multiple images of the same object captured from different angles (stereo photogrammetry), shadow analysis is the prime method when dealing

with a single image or single image angle (monoscopic photogrammetry), which is most useful in the limited data environment of adversarial military analysis. In the presiding literature, the term "shadow analysis" in both stereo and monoscopic photogrammetry is used to differentiate height estimation efforts from other aspects of photogrammetry.

A basic outline of the monoscopic photogrammetric method of shadow analysis can be found from Cordova (2005). Likewise, Adeline (2013) provides a review of various RS shadow measurement uses, identification methods and algorithms, and physical constraints. While property-based methods of shadow analysis rely on spectral imagery to evaluate radiance and reflectance of shadows, this thesis focuses more heavily on model-based shadow analysis. This method uses a geometric and physical approach to shadow analysis and aims to measure objects and their cast shadows; however, it requires situational information (angle of the sun, shadow surface orientation, etc.) as opposed to wider spectral bands (Adeline et al. 2013; Al-Najdawi et al. 2012; Shao et al. 2011).

The model-based method is also better suited for extracting physical information about a sensed object, such as height, through the trigonometric Equation 6 as follows (Larson 1993):

$$x \tan \theta = h \qquad (6)$$

where x is the known shadow length, θ is the angle of the sun's altitude (calculable from known time and location on Earth, and often embedded in digital imagery), and h is object height. While this method of height calculation is common in aforementioned research, McGlone (1994) performs additional analysis using oblique angle viewpoints rather than right-angle trigonometry, creating an automated shadow calculation and object identification tool.

Algorithms for shadow enhancement in aerial imagery (Liasis & Stavrou 2016) parallel advancements in shadow detection with small-scale ground-based sensors (Al-Najdawi et al

2012). Often, model-based studies are used to more accurately identify shadow location (Li et al 2005), while property-based methods provide more definite identification of shadow edges (Nagao et al 1979) and objects within shadows (Shimoni et al 2011).

There is also a blending of both forms by which radiance data is used to make shadows more identifiable for model-based analysis, while length identification is used to build better parameters in property-oriented image classification. The heights of ice-ridges were measured by Kwok (2014) using shadows from satellite imagery, with subsequent analysis by Miao (2016) creating a system of image classification for ice-ridges using these shadow-to-height measurements. One step further, Wegner (2014) use a variety of interferometric synthetic aperture radar (InSAR) measurements in combination with sun shadow lengths to build high-confidence object height estimations. Research has also been conducted into automated shadow removal from imagery in open source products like Google Earth using these same techniques (Guo et al. 2010; Kwatra & Dai 2012). Finally, Raju (2014) discusses issues with shadow visibility when performing shadow analysis in image classification studies. In this regard, there is a wealth of literature on shadow photogrammetry, though much is devoted toward image classification rather than object detection, such as this thesis's proposed application to radar structures.

2.6. GIS Studies of Military Radar

The majority of radar-related GIS non-RS studies regard location optimization problems, but still provide a baseline for how radar is measured by GIS in a military setting. Bell (2011) is heavily cited for this application of GIS, reviewing missile defense alert structures. In the study, alert radar coverages of targets are sought according to hierarchical target values, with free position of radar structures. In essence, this allows for the planning of radar defenses based on

known targets. Alkanat (2008), like others (e.g., Franklin et al 1994), applied similar methods as Bell toward surface-to-air missile (SAM) coverage in Turkey. Using defined targets with hierarchical value, Alkanat optimized locations for various SAM systems to ensure coverage. Straitiff (2010) performed a location optimization analysis of similar optimization problems using a less direct workflow. Staitiff's study theorizes optimal geometries of coverage, bounds this geometry to a target, and then performs adjustments to increase optimization within the new boundaries. Gonsalves (2003) outlined the use of GIS and optimization of weapon system interactions and provides geographic background to how radar in missile defense systems can best communicate and coordinate.

Studies have also been performed based on existing radar stations and their real or potential limitations. Kostic & Rancic (2003) modelled potential radar coverages in a virtual environment as 3D analysis against known digital elevation model (DEM) data. This served to build viewsheds and understand what a radar sensor might see in a given environment. Kucera (2004) performed an analysis of Guam's military radar stations with DEM data as well, creating viewsheds of expected radio wave propagation from various radar towers. Zemmari (2012) performed an analysis of potential maritime radar surveillance techniques with known radar towers positions and developed a method of ship tracking through overlapping radar coverages.

Nonetheless, no research exists using GIS or RS measurement to estimate maximum radar range via height calculation, as most mentioned studies either operate at too small a scale or too specific a scope to discuss potential maximums bounded by Earth's geometry. Additionally, few articles evaluate enemy defensive structures, let alone attempt to estimate an adversary's radar heights. Almost all works focus on radar systems that are either hypothetical or to which the researcher could potentially walk up in person. This thesis hopes to fill this gap, providing a

novel approach within the realm of geospatial intelligence tradecraft which combines RS, GIS, and geometry to solve radar range equations when radar heights are unknown.

Chapter 3 Methodology

Existing literature does not provide a clearly analogous case methodology for the proposed study. This may be in part due to the fusion of RS, raw math, and GIS into a single workflow. Additionally, the study requires prerequisite knowledge and interest in RS, radio propagation, and GIS. While Kostic & Rancic (2003) and Kucera (2004) focus on the role of elevation in radar LOS (3D and 2D, respectively), their studies plot existing radar sensors through known territory with potentially unlimited access to data and the sensors themselves, at ranges inside the radar horizon. The true novelty of this thesis is the application of a similar investigation in an environment without the issue of elevation change, but rather the issue of extremely limited access to radar sensors and structures. Similarly, this thesis focuses on maximum radar ranges limited by the curvature of the Earth rather than obstructions or radar signal loss.

The study area for this project consists of China's "Big Three" land reclamation sites. RS data was sourced from the DigitalGlobe Foundation, while CSIS/AMTI provided raw and analyzed information regarding weapon systems and radar positions on the islands. Imagery from DigitalGlobe was sourced in part from the GeoEye and WorldView satellite platforms. These data were used for shadow analysis and trigonometric measurement of tower heights within a GIS platform. Radar horizon calculations were then performed, adjusted for the geoclimatic factor K. Data produced were measured as vector ranges of radar horizons for comparison with various other weapon system ranges and with initial radar range estimates by CSIS/AMTI. This methodology therefore provided an experimental approach to be used in later studies of other radar sites in the SCS or similar environments.

This study used a combination of techniques and manual measurements rather than an automated, modelled approach. Results were analyzed based on shared coverage with other A2AD systems, and subsequently evaluated the accuracy of CSIS/AMTI estimations.

3.1. Data

Three data categories were used in this methodology. Imagery data was used to perform shadow photogrammetry. Weapon system ranges and radar range estimations from CSIS/AMTI and other researchers was used as baseline coverages for comparison with those calculated in this study. Geospatial data was largely created through this study, rather than used as an input, but nonetheless served as vital reference.

3.1.1. Imagery

Imagery for this project was provided by the DigitalGlobe Foundation, ranging in maximum ground sampling distance (GSD) for multispectral imagery at 1.24 to 1.84 m. The georeferenced raster imagery was imported into ArcMap and overlayed with basemap imagery of the region to ensure that any obvious georeferencing errors could be found and corrected. Measurements taken from the imagery were measured in meters, with the imagery projected to WGS 1984. Imagery can be seen in Figure 9 with higher scale inset to display resolution size.

Radar towers, previously identified by CSIS/AMTI as seen in Figure 10, were matched to imagery in from the DigitalGlobe Foundation with recorded date and time. This information, combined with geographic location, was calculated by the data provider and included with the altitude angle of the sun in the imagery's metadata.

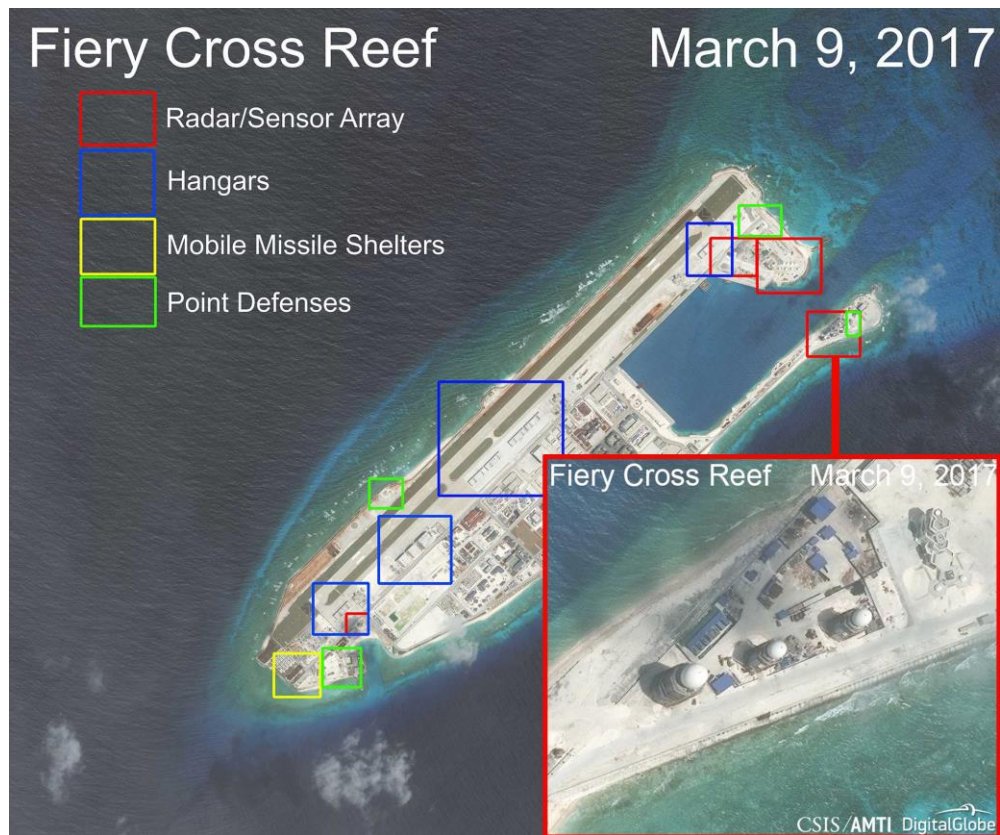*Figure 9: 1:1,250 and 1:23,000 Scale of Radar Array. Satellite image(s) courtesy of the DigitalGlobe Foundation.*

Figure 10: CSIS Identification of Island Features, with Inlay of Radar Array.

3.1.2. Weapon System Data

Various other weapon systems further down the A2AD "kill chain," as discussed in Chapter 2, were also vital for measurement in this study. As the tools enabled by radar warning systems, they have an integral relationship with radar. The ranges of these tools and of radar surveillance work together to match field of vision to field of response. The data in Table 1 describes the ranges of these tools as deployed by China in the SCS, some of which have already been identified in the Spratlys and Paracels, and others yet suspected.

Table 1: PRC Weapon System Ranges

**Reported Range Estimation, (Ashdown 2016; Gormley et al 2014; Kable Intelligence, CSIS/AMTI)**

System	Type	Range
HQ-9	Surface to Air Missile	230km
YJ-62	Anti-Ship Missile	400km
J-10	Fighter Aircraft	550km
Radar	High Frequency	300km
Radar	Conventional	50km*

3.1.3. Geospatial Data

Geospatial shapefiles stored in .kmz format were also supplied via public hosting by CSIS; however the data was deemed inappropriate for this project's use due to its low quality. Within the data was missing key island centroids, including Subi Reef, and appeared to be derived from dated Google Maps GPS coordinates. These coordinates roughly note the location of natural reef chain features, but do not accurately represent the new land reclamation features on specific segments of often sprawling reefs. For this reason, visual centroid approximation was manually created for the sake of developing island centroids, seen in Figure 11. This manual

approximation was used due to the lack of geospatial data for the islands, including polygonal area shapefiles, due to the limited age of the artificial islands. These centroid locations can be found in Appendix A.
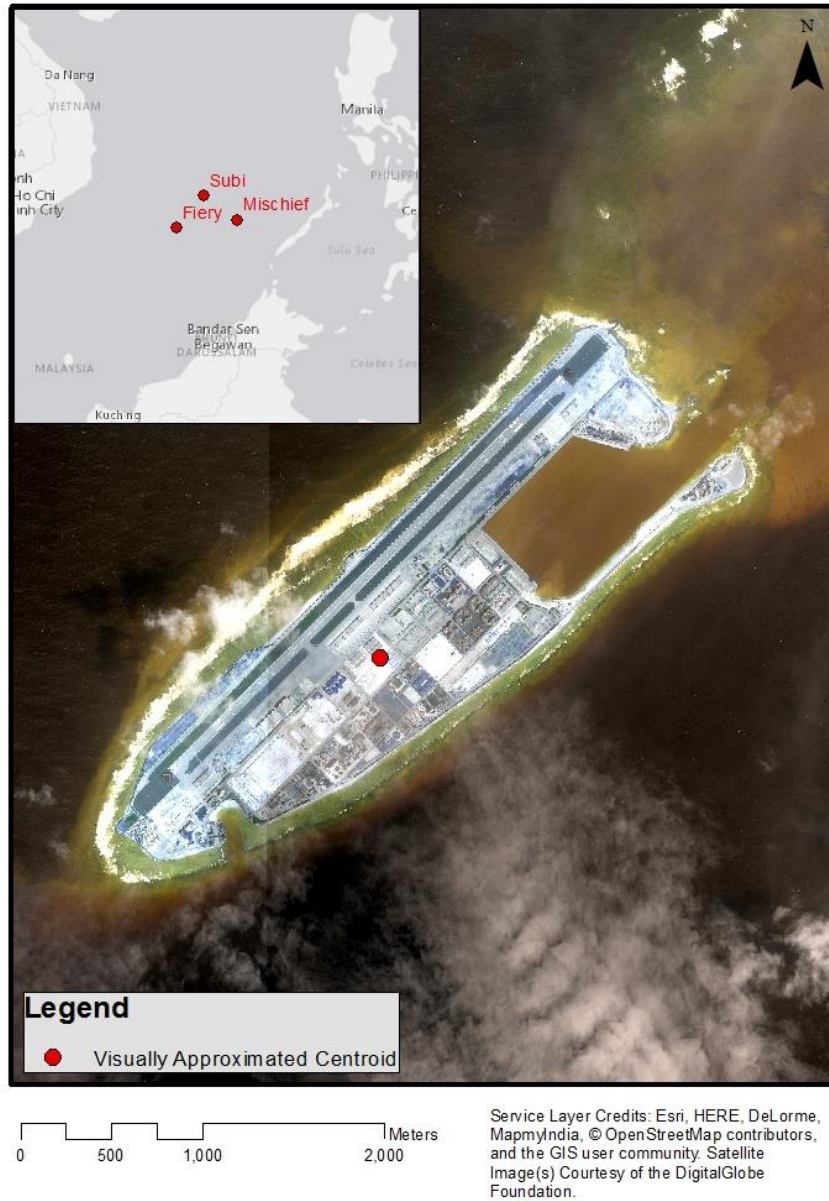
Figure 11: Fiery Cross Reef, Manual Centroid Creation. Centroids were created based on visual centers due to lack of geospatial data. Satellite image(s) courtesy of the DigitalGlobe Foundation

3.2. Procedure

With these data, the project followed the research design detailed in Figure 10, whereby data from CSIS/AMTI and the DigitalGlobe Foundation was re-analyzed for greater accuracy of radar ranges using the notion of radar horizons. This project had four main phases: (1) data was gathered, catalogued, and organized; (2) shadow analysis was performed to calculate radar heights for each tower and these heights were then used to calculate radar horizons at various altitudes; (3) these data were integrated into a GIS with new buffers created for other weapon systems to match CSIS/AMTI publishing; and (4) these coverages were analyzed for comparison with each other and with initial CSIS/AMTI radar range estimations.

3.2.1. Data Preparation and Preprocessing

Before the main analysis could be performed, available data was gathered and integrated into a GIS (see procedural workflow in Figure 13). Satellite imagery from the DigitalGlobe Foundation was overlaid against open source basemap data to ensure correct georeferencing. This imagery was subsequently cross-referenced with CSIS/AMTI identification of radar array locations as seen in Figure 10. Centroids for the data were needed, but could not be gathered from existing sources and were therefore created manually as discussed below.

Radar array zones and their locations were matched and marked in the data for subsequent analysis (see Figure 14), with GPS coordinates recorded in Microsoft Excel spreadsheets for quick integration into any GIS or RS software system. Red, Green, and Blue light bands embedded in the imagery were also adjusted manually to enhance visibility of each individual shadow for the measurements that followed.
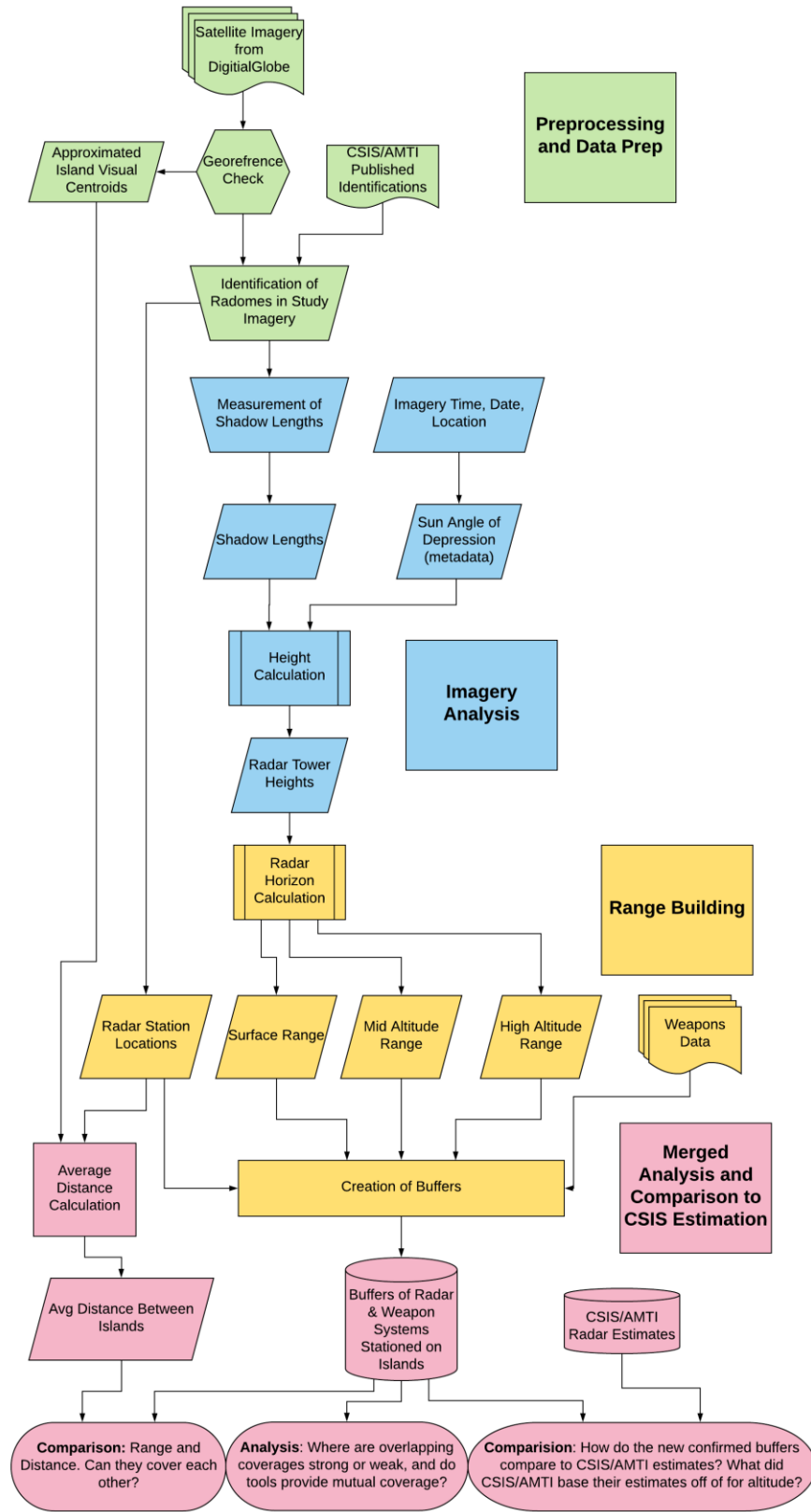
Figure 12: Project Methodology, showing four phases of project structure (labelled in bold) by color-coding.
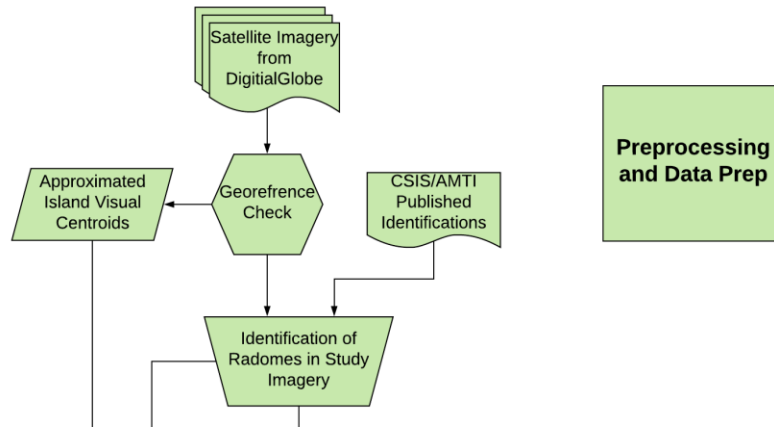
Figure 13: Data Preprocessing and Integration Model

Figure 14: Zone FC2. Compare to Figure 10. Satellite image(s) courtesy of the DigitalGlobe Foundation.

Each zone of radar arrays identified by CSIS/AMTI was examined and confirmed to be a conventional radar tower array rather than an "Elephant Cage" or antenna picket OTH/HF system. In total, this left six relevant zones, as identified by Figures 15, 16, and 17. Red-marked "Radar/Sensor Array" zones not included depicted OTH/HF radar systems. In total, these zones identified 13 individual radar towers for measurement. Each zone can be viewed individually in Appendix B.

Due to the high volume of data provided by the DigitalGlobe Foundation, imagery that did not contain relevant sites was removed from the GIS to increase processing speed. Additionally, panchromatic imagery was discarded due to the ease in identifying shadows with the visible spectrum. This reduced the imagery load from nearly 50 GB to below 0.5 GB, including relevant shapefiles for georeferencing and image tile schemes; however, this also removed higher resolution imagery which may have been useful for purposes other than shadow detection (see Appendix A). Towers and their sites identified by this process are listed in Table 2.

3.2.2. Imagery Analysis

With the imagery prepared and catalogued, and each individual radar tower plotted by GPS coordinates, shadow analysis was then performed, as articulated by the workflow in Figure 18. This methodology uses Equation 6 as described in Chapter 2 to calculate tower heights from satellite imagery from Worldview 3, Worldview 4, and GeoEye 1 sensor platforms provided by the DigitalGlobe Foundation.

Table 2: Tower Imagery Locations

Tower ID	Zone ID	Island	Satellite	Image ID	Tile	Latitude (m)	Longitude (m)
01	FC1	Fiery Cross Reef	WV03	105001000D959600	R1C2	12,567,841.05	1,069,124.62
02	FC2	Fiery Cross Reef	WV03	105001000D959600	R2C2	12,568,344.31	1,068,654.97
03	FC2	Fiery Cross Reef	WV03	105001000D959600	R2C2	12,568,401.71	1,068,674.30
04	FC2	Fiery Cross Reef	WV03	105001000D959600	R2C2	12,568,451.38	1,068,690.07
05	FC3	Fiery Cross Reef	WV03	105001000D959600	R2C1	12,565,786.80	1,067,039.70
10	S1	Subi Reef	GE01	10400100355E1900	R2C2	12,697,999.46	1,222,614.46
11	S2	Subi Reef	GE01	10400100355E1900	R2C2	12,697,924.91	1,221,676.88
12	S2	Subi Reef	GE01	10400100355E1900	R2C2	12,697,980.48	1,221,667.35
13	S2	Subi Reef	GE01	10400100355E1900	R2C2	12,698,036.04	1,221,658.62
21	M1	Mischief Reef	WV04	9929b355-14fa-42e7-8408-41338ef178d9-inv	R4C2	12,862,204.50	1,110,205.25
22	M2	Mischief Reef	WV04	9929b355-14fa-42e7-8408-41338ef178d9-inv	R3C3	12,857,356.88	1,107,451.42
23	M2	Mischief Reef	WV04	9929b355-14fa-42e7-8408-41338ef178d9-inv	R3C3	12,857,408.21	1,107,472.76
24	M2	Mischief Reef	WV04	9929b355-14fa-42e7-8408-41338ef178d9-inv	R3C3	12,857,458.22	1,107,495.09
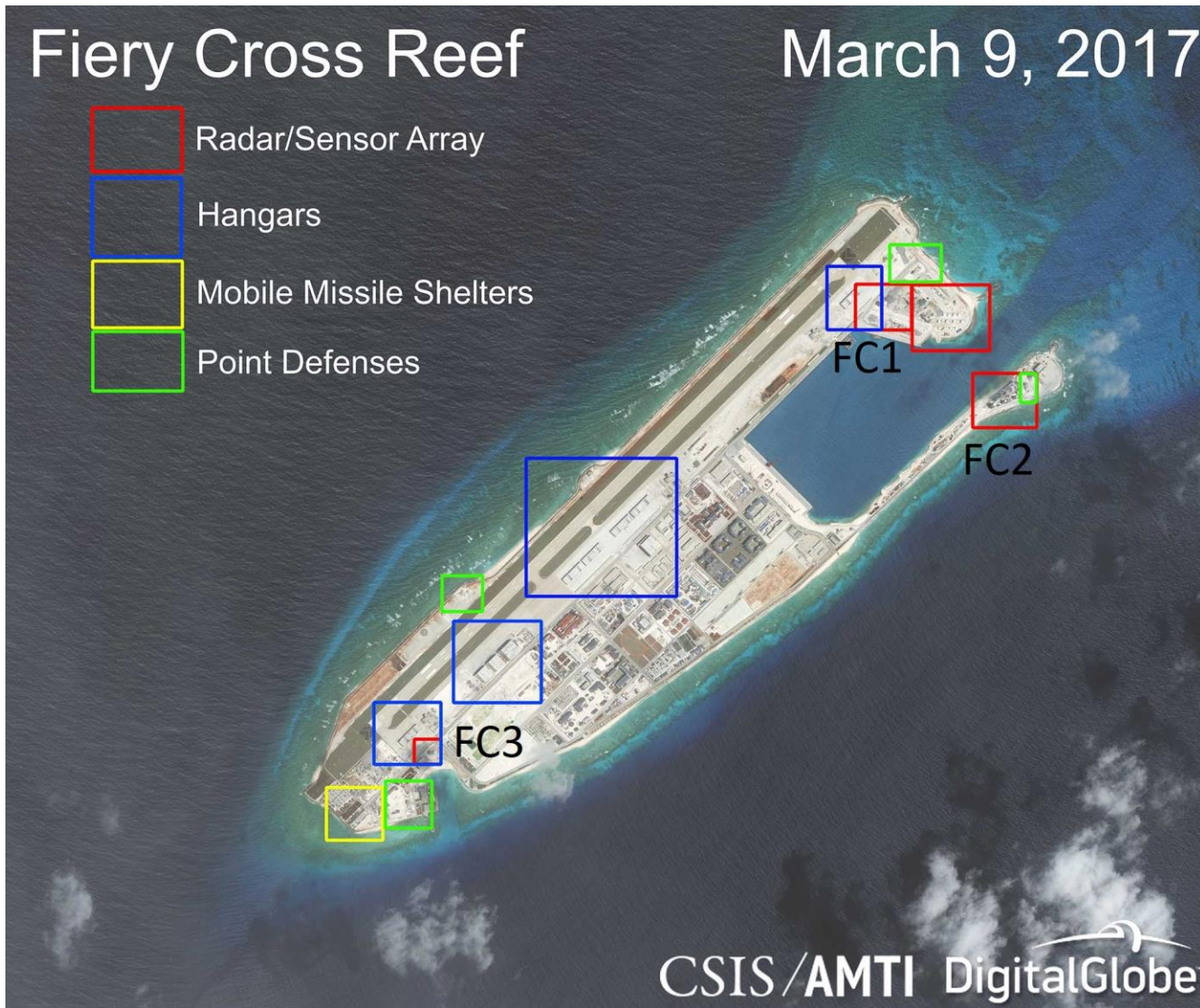
Figure 15: Fiery Cross Reef Radar Zones
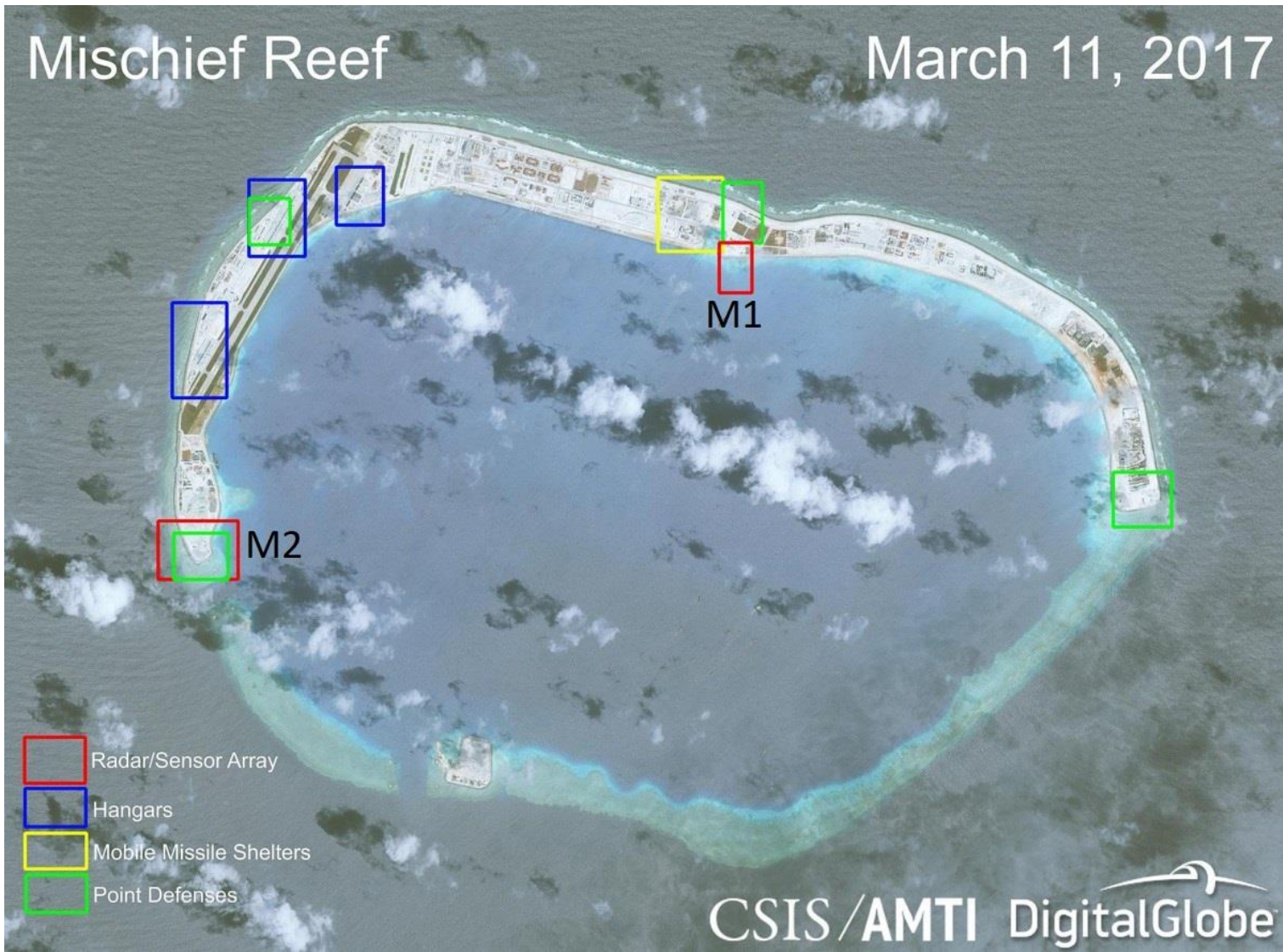
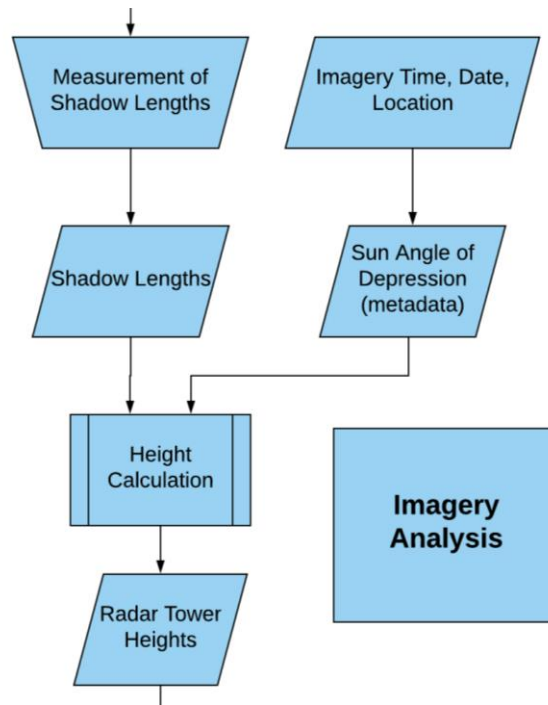*Figure 16: Mischief Reef Radar Zones*

Figure 17: Subi Reef Radar Zones

Figure 18: Imagery Analysis Model

From identified radar towers in the imagery, building shadow lengths were manually measured in meters using ArcMap's Measure tool (see Figure 19). These measurements were rounded to the nearest tenth of a meter then compiled with imagery metadata for date and time, and with the precise location of the tower measured. These data can be seen in Table 3. Rounding for shadow lengths was applied to decrease the effects of any measurement error. These calculations were compiled in a standard Microsoft Excel spreadsheet in .xlsx format linked to the project's ArcMap document. Calculations were performed using the following syntax:

[Photogrammetric Height] = [Shadow Length]*TAN(RADIANS ([Solar Altitude])) (7)

This syntax includes adjustments to ensure that degrees and radians were properly calculated given the sun's altitude in angle degrees.
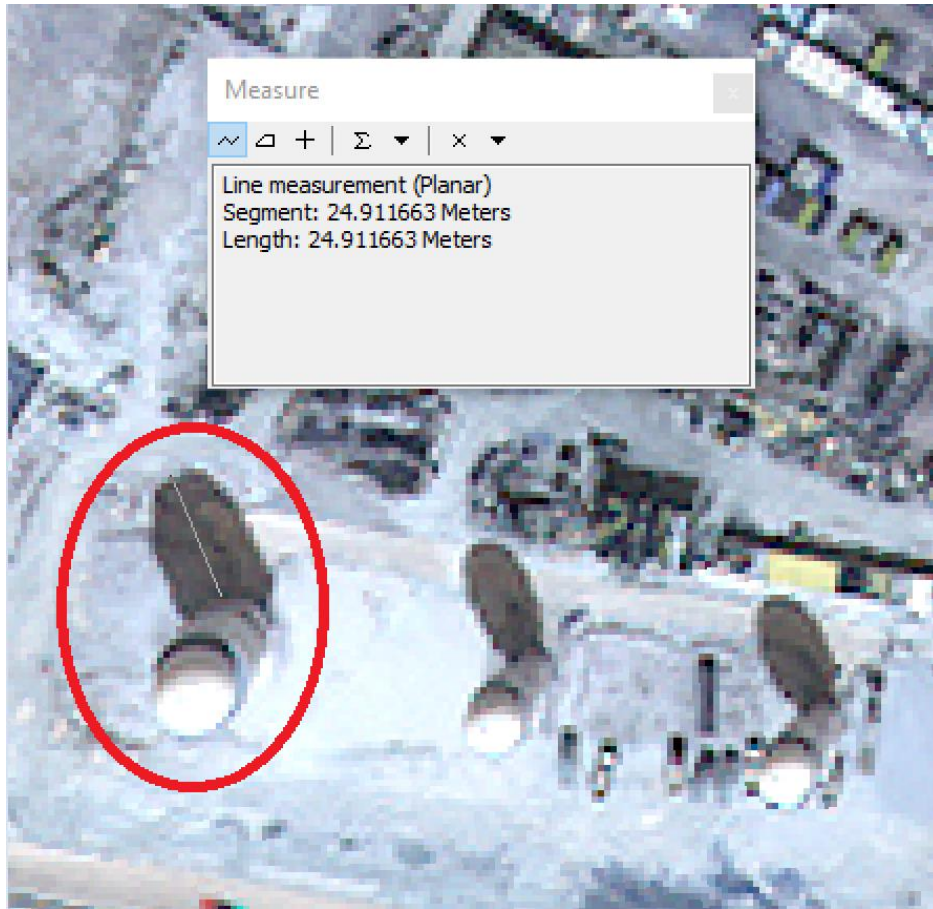
Figure 19: Example Shadow Measurement in Multispectral Imagery. Satellite image(s) courtesy of the DigitalGlobe Foundation.

To accurately measure the height of radar towers, the height from the base of the tower on land above sea level was additionally measured and added to the overall height. Rather than create a formal elevation model, this study estimated the altitude of island surfaces based on tide changes in the region. Assuming the surfaces of pre-planned, man-made islands were at least one meter above the maximum tide in the region, one meter was added to the highest diurnal high tide mark for the Spratly chain for the month of imagery capture, at 0.6 m, for a total of 1.6 m added (Brainware n.d.). This value estimates tide heights based on sensor data throughout the region, which share tidal rhythms (Yanagi et al. 1997). Likewise, while the exact location of the

radar sensor within the domed cover atop each structure is unknown, this study assumes the

highest possible point possible.

Table 3: Tower Height Measurements and Height Calculations

Tower ID	Shadow Length	Sun Altitude Angle	Photogrammetric Height (m)	Absolute Height (m)
01	34.8	51.7	44.06	45.66
02	25.4	51.7	32.16	33.76
03	21.4	51.7	27.10	28.70
04	20.6	51.7	26.08	27.68
05	30.4	51.7	38.49	40.09
10	23.1	53.6	31.33	32.93
11	24.9	53.6	33.77	35.37
12	21.7	53.6	29.43	31.03
13	21.3	53.6	28.89	30.49
21	28.8	50.7	35.19	36.79
22	25.8	50.7	31.52	33.12
23	22.2	50.7	27.12	28.72
24	23.1	50.7	28.22	29.82

3.2.3. Buffer Creation

These heights formed the core data set for radar range analysis as discussed in Chapter 2.

The first step to confirming radar ranges was to calculate ranges for various altitudes using

Equation 3 and 4. For geospatial analysis, these ranges and other data were converted to buffers

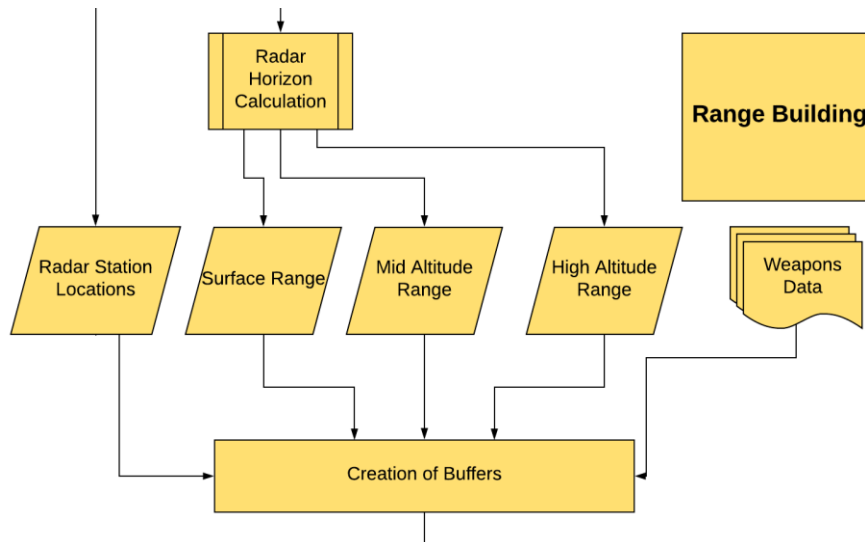based on range and location of origin as displayed by Figure 20.

Figure 20: Buffer Creation Model

To calculate appropriate radar horizon ranges (or radar LOS) Equation 4 was used in the previously mentioned linked Excel table. To yield results in meters, the calculation was adjusted to the following final syntax:

[Range] = 4.12*((SQRT([Absolute Height])+SQRT([Investigated Altitude])))*1000   (8)

where the Investigated Altitude was adjusted to 0; 3,000; and 10,000 respective of Surface, Mid, and High Altitudes. The reciprocal equation (Equation 5) was subsequently used to reverse CSIS/AMTI assumed ranges in the following syntax, which was used to calculate both minimum tower heights for a given altitude and range, and to calculate minimum visible altitude for a given tower height and range:

[Unknown Height] = (([Range]/4.12)-(SQRT([Known Height])))^2   (9)

Using locations specific to each radar tower, buffers were created based on respective tower height for Surface (0 m), Mid Altitude (3,000 m), and High Altitude (10,000 m) ranges, seen in Table 4. Additionally, other weapon system data was used to create buffers based on island centroid locations, using ranges as previously discussed in Table 1.

Buffers were created using the Buffer (Analysis) tool in ArcGIS, selecting field values for buffer distance, thus creating a unique buffer for each tower depending on its unique radar horizon (see Figure 21). This process was repeated for each altitude ("Surface" at 0 m, "Mid Altitude" at 3,000 m, and "High Altitude" at 10,000 m) creating 39 unique buffers in three shapefiles. These undissolved buffers were created primarily for visualization.

Table 4: Radar Horizon Ranges at Various Altitudes

Tower ID	Range at Surface Altitude (km)	Range at 3,000m Altitude (km)	Range at 10,000m Altitude (km)
01	27.84	253.50	439.84
02	23.94	249.60	435.94
03	22.07	247.73	434.07
04	21.68	247.34	433.67
05	26.09	251.75	438.09
10	23.64	249.30	435.64
11	24.50	250.17	436.50
12	22.95	248.61	434.95
13	22.75	248.41	434.75
21	24.99	250.65	436.99
22	23.71	249.37	435.71
23	22.08	247.74	434.08
24	22.50	248.16	434.50
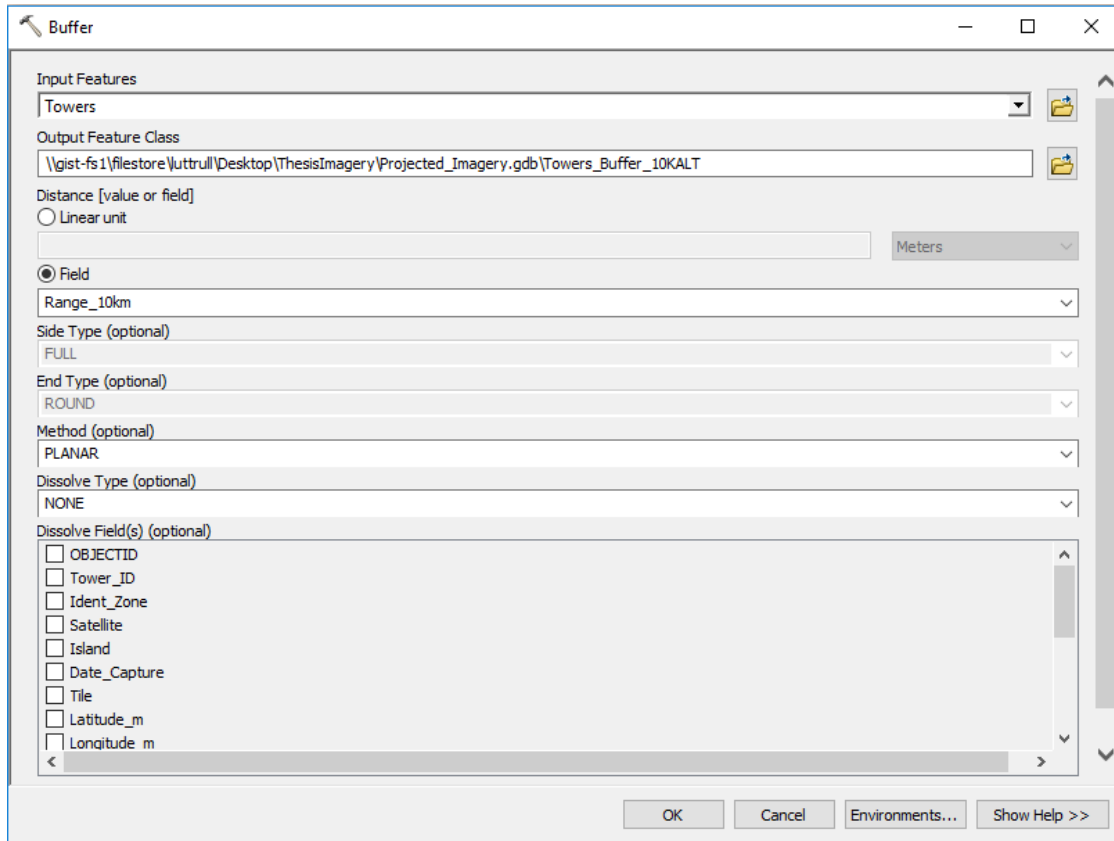
Figure 21: Buffer Selections

Further buffers were created to compare area coverage between varying radar horizon estimations and calculation methods. These dissolved buffers consisted of a single polygon whose area could be measured for the collective of all towers. This area data was extracted from the automatically generated attribute table.

3.2.4. Combined Analysis

These buffers were then overlaid for a combined analysis (modeled in Figure 22). An average distance between each of the island's centroids was measured using the Point Distance Tool, which averaged to 234,014.4 m from one island centroid to the another.
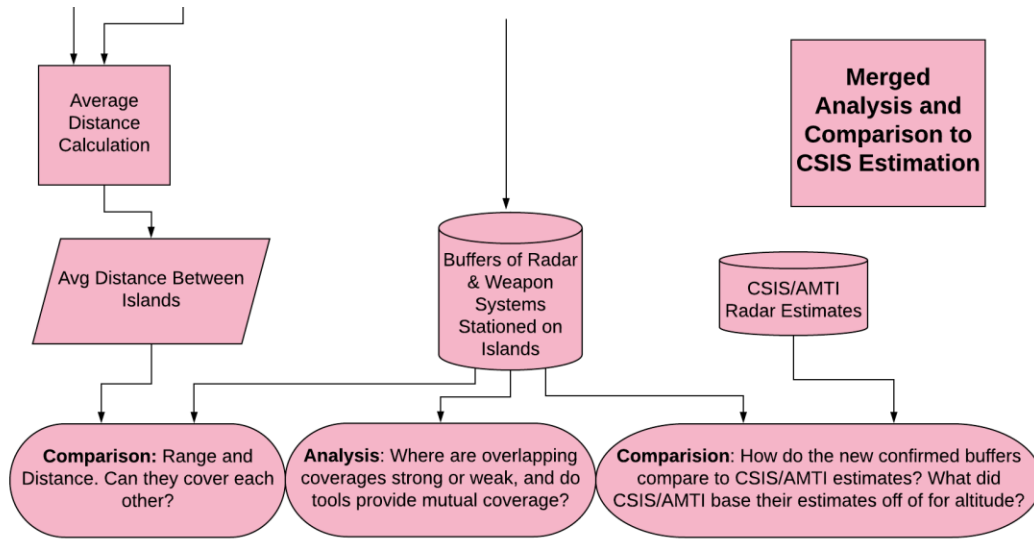
Figure 22: Combined Analysis Model

To geospatially compare for area coverage, location coverage, and overlap against data previously published by CSIS/AMTI, the average measured height of the radar towers was used to calculate radar horizon ranges, measured in buffer from the island centroid (see Table 5). To this end, the approximated island centroid was used as the buffer input for all other systems mentioned in Table 1. An additional buffer was created using the CSIS/AMTI conventional radar range estimate, centered around observed tower locations used in this study. This was done for equal comparison of coverages.

Table 5: Ranges Derived from Average (Mean) Tower Height

Average Tower Height (m)	Range at Surface Altitude (km)	Range at 3,000m Altitude (km)	Range at 10,000m Altitude (km)
33.40	23.81	249.47	435.81

No other statistics, such as standard deviation, were drawn from the table of tower heights, due to the clear variety of tower sizes in the imagery. As there was no standardized size, statistical approaches to more accurate tower height estimation would be highly vulnerable to skew.

Chapter 4 Results

The maps and analysis in this chapter utilize data and methodologies discussed in Chapter 3 to prove the efficacy of this thesis's proposed model of shadow analysis for radar horizon estimation, and for comparison of the described model's output against previous published estimates by CSIS/AMTI. Chapter 5, alternatively, discusses the accuracy and shortcomings of this methodology and case study. It should be noted now, however, that much of this study relied on manual processes including measurements and visual approximations due to the lack of geospatial data available for such recently created features.

Overall, the methodology successfully provided necessary geospatial data to improve and update previous radar range estimates with more precise calculations. There were noticeable differences between this methodology's results and those of previous estimates. Due to the negatively exponential nature of the involved math, however, these differences converged as scale increased.

4.1. Coverage Results

The measurement of radar horizons, based on shadow-to-height and LOS calculations detailed in Chapter 2, resulted in calculated areas of coverage for every inspected radar tower. As outlined in Chapter 3, tower heights were calculated using Equation 6; radar horizons were subsequently calculated using Equation 4. All reverse analysis for unknown heights used Equation 5. Coverages based on this project's methodology for radar horizon calculation are found in Figure 23. These calculations are also recorded in Table 4. Additionally, the average tower height was used to create buffers centered from the approximated island centroids (see Figure 11). This data, visualized in Figure 24, acts as a simpler approximation of data found in Figure 23.
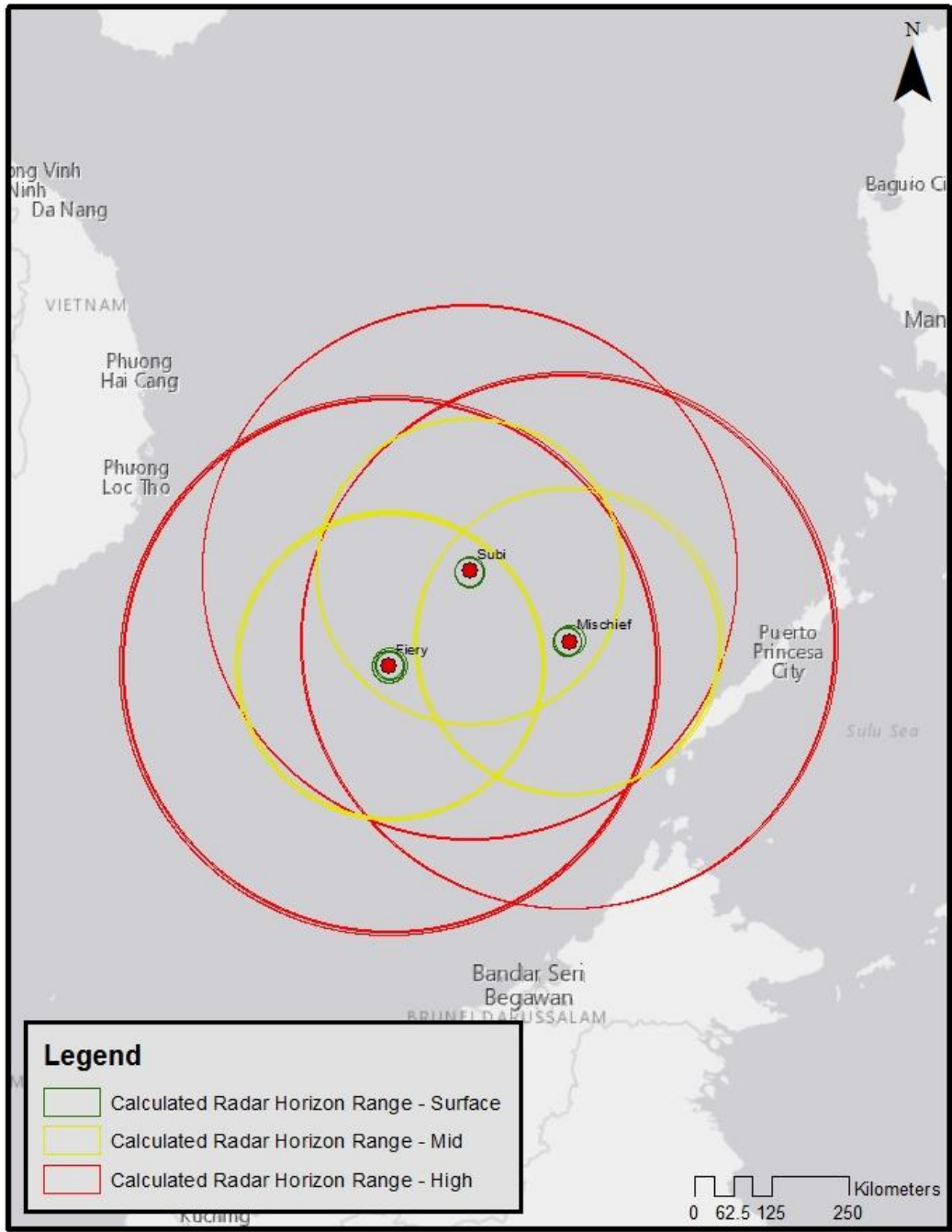
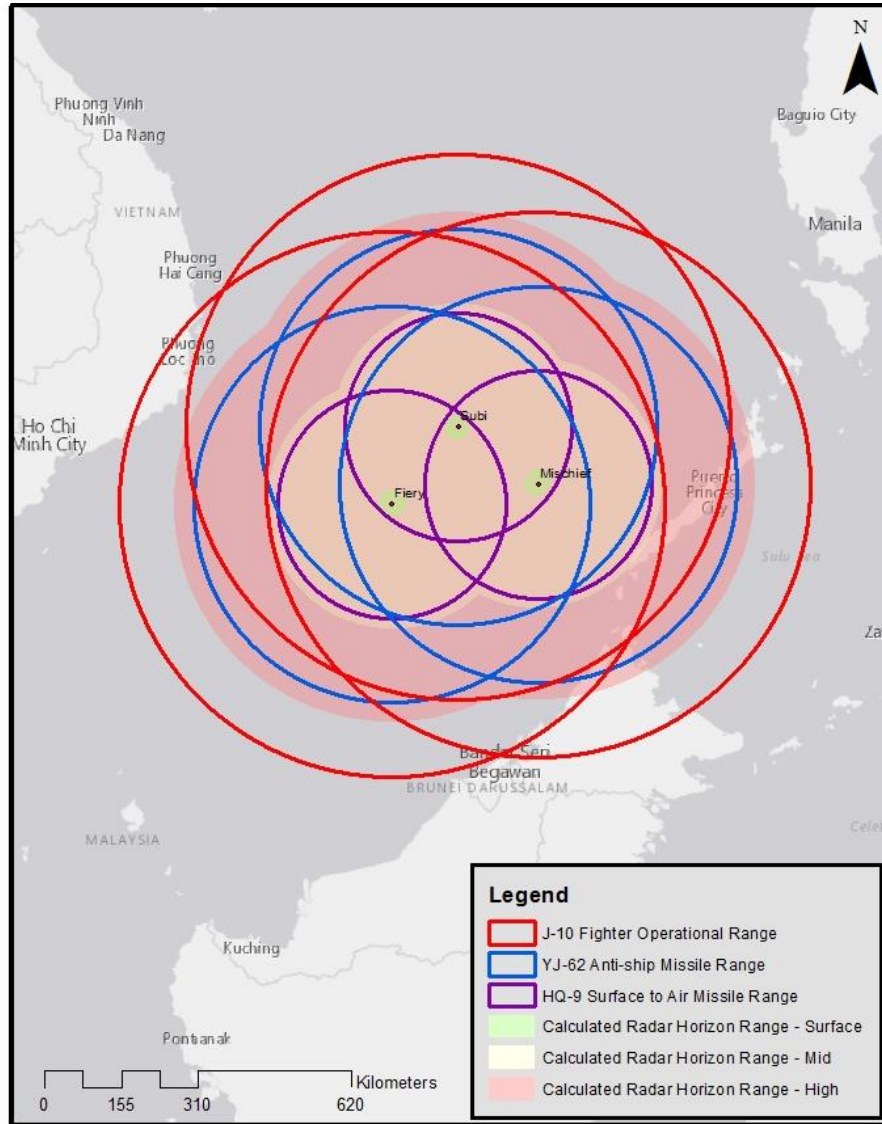*Figure 23: Final Radar Horizon Calculations from Shadow Analysis Method*
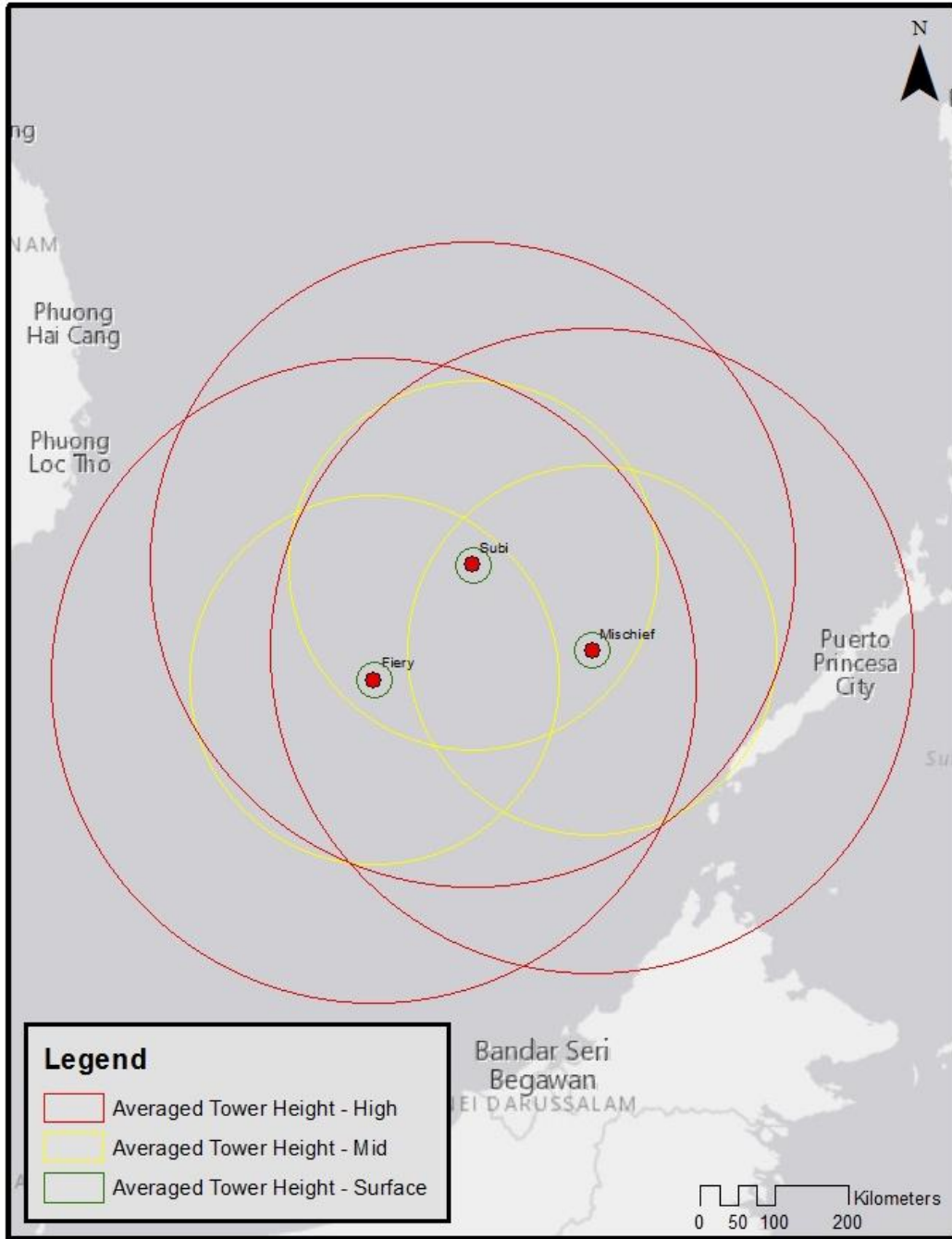
Radar buffers drawn from precise tower locations. Radar Horizon Ranges calculated assuming 0m altitude for "Surface"; 3000m altitude for "Mid"; and 10000m altitude for "High". Each range calculated per individual tower height. Weapon system buffers drawn from island centroids based on data found in Table 1.

Service Layer Credits: Esri, HERE, DeLorme, MapmyIndia, © OpenStreetMap contributors, and the GIS user community. Satellite Image(s) Courtesy of the DigitalGlobe Foundation.

Figure 24: Radar Horizons Calculated Using Average Tower Height and Island Centroids

4.1.1. General Assessment of Coverage

The buffers of newly calculated radar horizons were additionally overlaid with buffers

created for reported A2AD weapon systems, as visualized in Figure 25 below.

Figure 25: Compiled Map of Calculated Radar Horizons & Other A2AD Weapon Systems

While almost every tool deployed on one island was covered by its own kind from a

neighboring island, this resulted in a triple coverage for all tools except the HQ-9 surface to air

missile. Fiery Cross Reef and Mischief Reef islands were reliant on Subi Reef for secondary coverage of HQ-9 anti-air defense.

4.1.2. Gap Estimation

There are clear and noticeable gaps in coverage between radar ranges. Using the averaged tower height and averaged island distance, radar towers leave 186.4 km unmonitored surface (0 m altitude) between each island. However, this observational blind spot could be monitored by radar coverage from unmeasured islands discussed in Chapter 1, or from OTH/HF radar, as seen in Figures 29 and 30.

4.1.3. Horizons at Fixed Distance

Given the averaged distance between each island, the radar horizon altitude was calculated using the average tower height via Equation 5. The resulting altitude, 2603.09 m, is within the "Mid Altitude" boundary of 3,000 m. This indicates that on average, each island is capable of observing all altitudes at or beyond Mid Altitude directly above each other island.

4.2. Radar & Weapon System Cooperation & Range Comparison

While radar is the first link in the A2AD "kill-chain," and the primary focus of this study, the tool's interaction with other A2AD systems is vital for comparison. With shared ranges, the tools may work together to successfully cooperate. Radar observation may aid weapon targeting or may alert personnel and automated systems of a target's existence in the first place. The following Figures 26-29 visualize the comparative coverages of known weapon system ranges, discussed in Table 1, with this study's calculated radar horizons. For independent mapping of weapon systems reported by CSIS/AMTI on Fiery Cross, Mischief, and Subi Reef, see Appendix C.
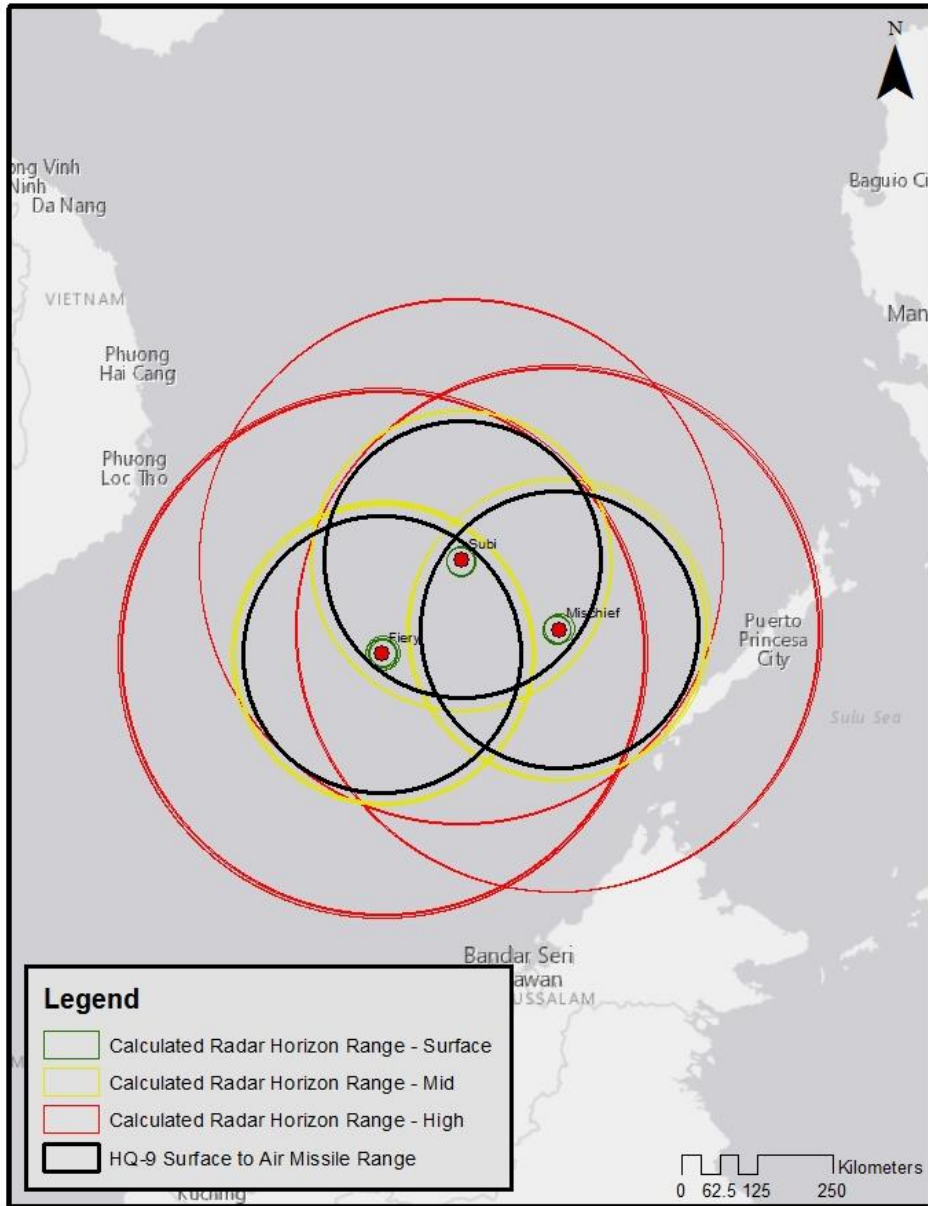
Radar buffers drawn from precise tower locations. Radar Horizon
Ranges calculated assuming 0m altitude for "Surface"; 3000m
altitude for "Mid"; and 10000m altitude for "High". Each range
calculated per individual tower height. Weapon system buffers
drawn from island centroids based on data found in Table 1.

Service Layer Credits: Esri, HERE, DeLorme,
MapmyIndia, © OpenStreetMap contributors,
and the GIS user community. Satellite
Image(s) Courtesy of the DigitalGlobe
Foundation.

Figure 26: Calculated Radar Horizons & HQ-9 SAM Ranges

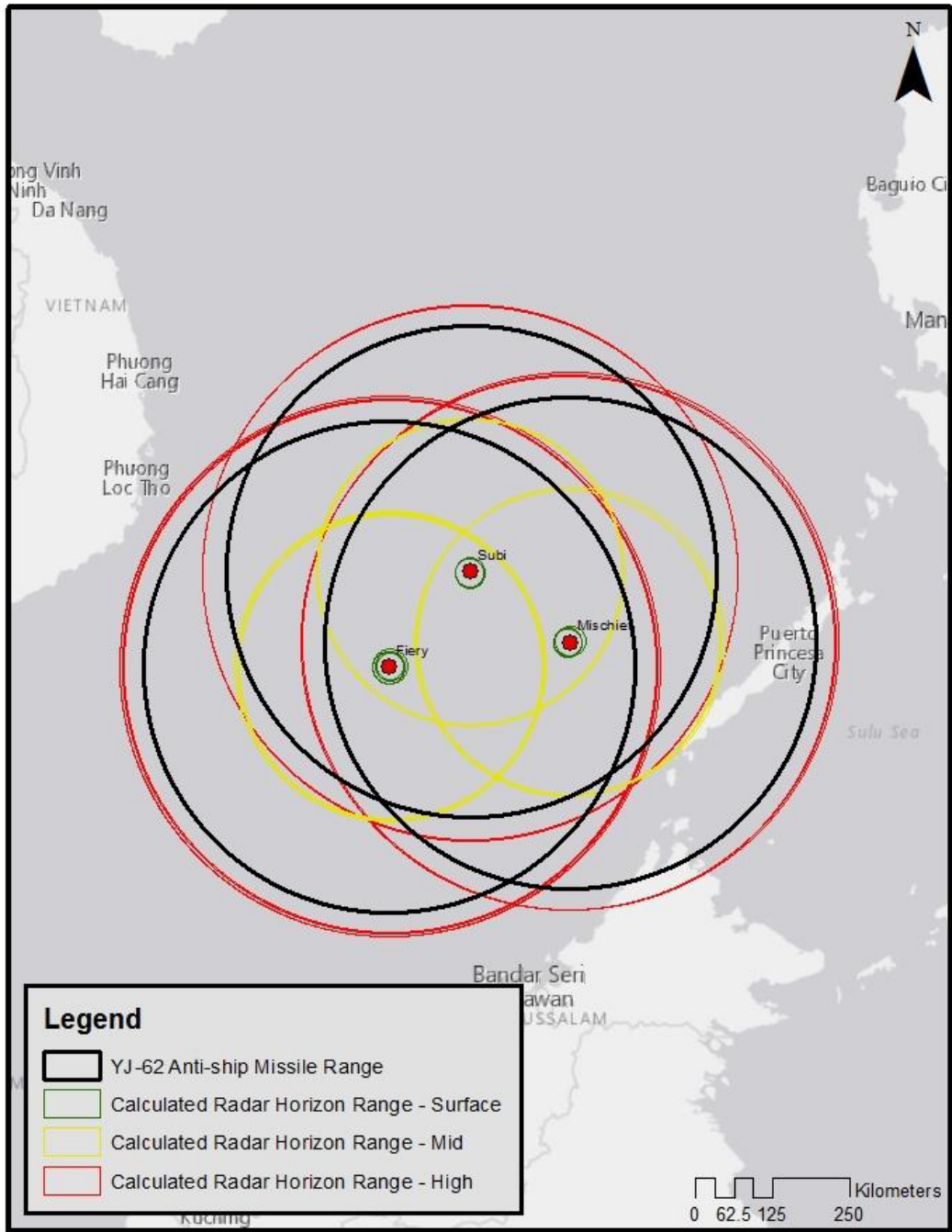*Figure 27: Calculated Radar Horizons & YJ-62 ASM Ranges*

Radar buffers drawn from precise tower locations. Radar Horizon Ranges calculated assuming 0m altitude for "Surface"; 3000m altitude for "Mid"; and 10000m altitude for "High". Each range calculated per individual tower height. Weapon system buffers drawn from island centroids based on data found in Table 1.

Service Layer Credits: Esri, HERE, DeLorme, MapmyIndia, © OpenStreetMap contributors, and the GIS user community. Satellite Image(s) Courtesy of the DigitalGlobe Foundation.

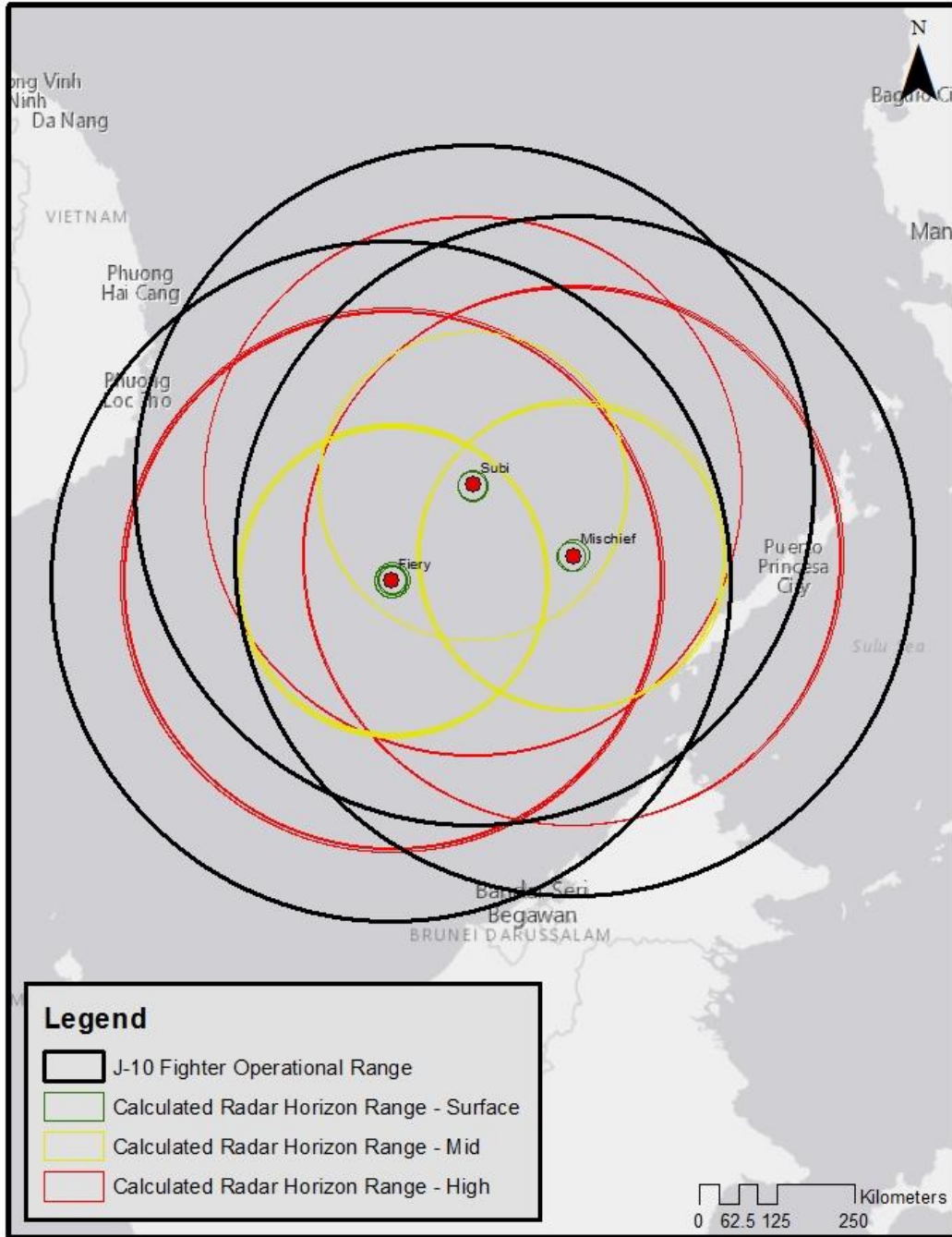*Figure 28: Calculated Radar Horizons & J-10 Fighter Operational Ranges*

Radar buffers drawn from precise tower locations. Radar Horizon Ranges calculated assuming 0m altitude for "Surface"; 3000m altitude for "Mid"; and 10000m altitude for "High". Each range calculated per individual tower height. Weapon system buffers drawn from island centroids based on data found in Table 1.

Service Layer Credits: Esri, HERE, DeLorme, MapmyIndia, © OpenStreetMap contributors, and the GIS user community. Satellite Image(s) Courtesy of the DigitalGlobe Foundation.
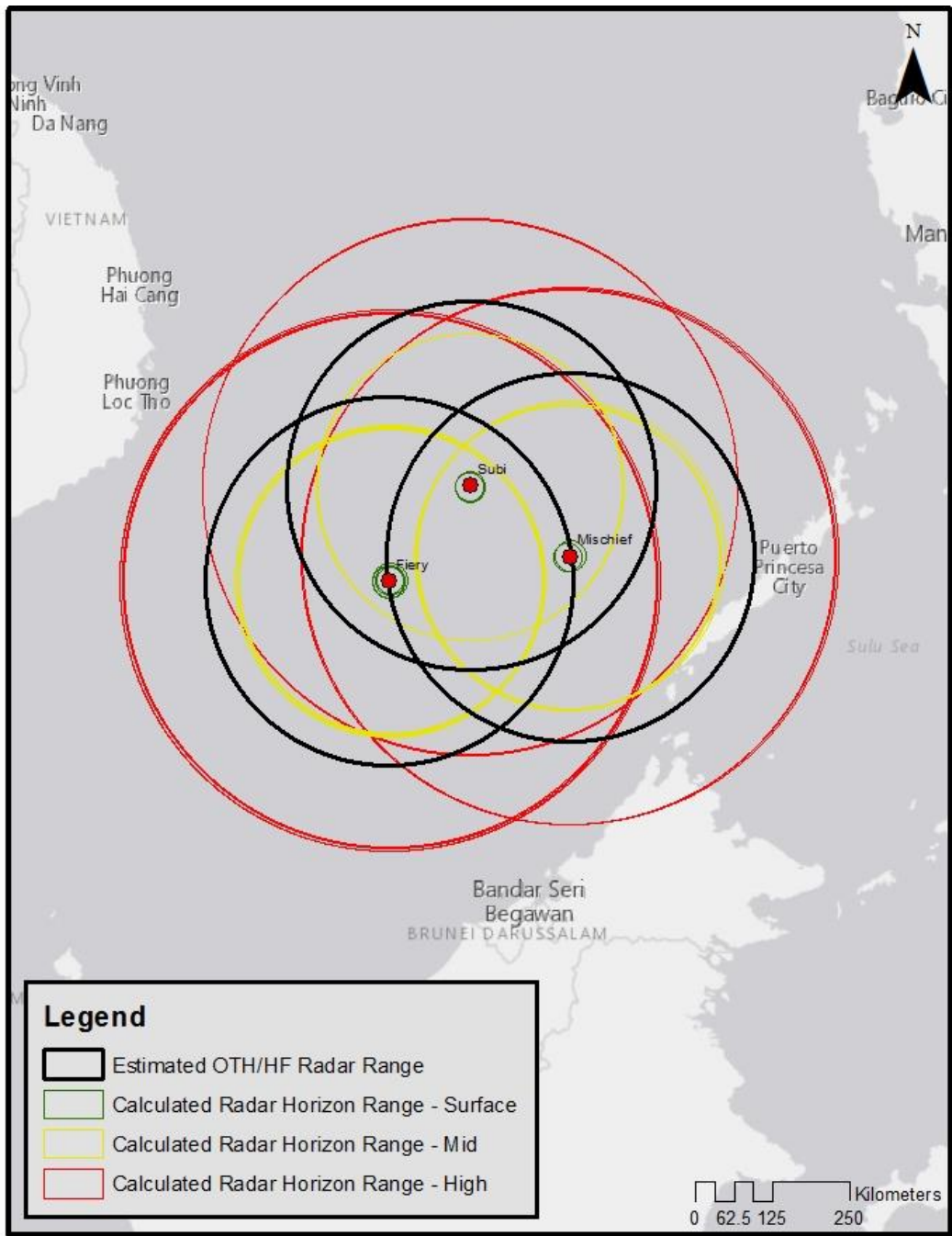
Figure 29: Calculated Radar Horizons & Estimated OTH/HF Radar Ranges

4.2.1. Assessment of Overlap

Calculated radar horizons exceeded HQ-9 SAM ranges at the Mid Altitude bracket, meaning that the entirety of the HQ-9's potential range launched from Fiery Cross, Mischief, or Subi Reef would be within radar observation above 3,000 m altitude. Using Equation 5 and the average tower height, the radar horizon at the HQ-9's maximum reported range is 2504.61 m altitude.

While the calculated radar horizons encompassed reported ranges for the YJ-62 anti-ship missile system, conventional aerial radar is of little use for this tool. Anti-ship missiles naturally target surface-traversing ships, rather than airships or other objects far above the surface of the Earth. To this end, Equation 4 was used to calculate the radar horizon for a 15 m tall object, such as an arbitrarily-heighted ship, using average tower heights. The resulting 39.7669 km distance is well within the YJ-62's range, leaving longer distances to targeting through OTH/HF radar or observation by other means.

The longest-range weapon system included in this study, the J-10 Fighter Aircraft, vastly exceeded the radar horizon ranges of radar towers measured on Fiery Cross, Mischief, and Subi Reefs. While the unloaded range of the aircraft is reported by Kable Intelligence to be 1,850 km, the operational, or combat, range of the aircraft was used at 550 km. At the edge of the J-10's operational range from one of the study's focused islands, the radar horizon for an average height radar tower is 16311.37 m altitude. This altitude nears the operational flight ceiling of the aircraft.

OTH/HF radar stands as the only other observational tool included in this study. While the maximum range reported by CSIS/AMTI is dubious due to the wide variation in ranges for OTH/HF (see Chapter 2), the published 300 km range was compared to calculated radar horizon ranges seen in Figure 29. Using Equation 5 and for an average height radar tower, the radar

horizon at the published OTH/HF radar range is 4493.88 m altitude. Practically, outside of 300 km distance from this study's island foci, all targets below this altitude would be unobservable by both radar methods when measured by this study's calculation and accepted estimates.

It should also be noted that OTH/HF range estimations created overlapping coverage of each island by both other Big Three bases. Though only by narrow margins (see Figure 30) Fiery Cross Reef (inset) and Mischief Reef OTH/HF exceed their separation distance and provide coverage for one another. This indicates a preplanning of island creation, or, more likely, a convenient choice of range estimate.
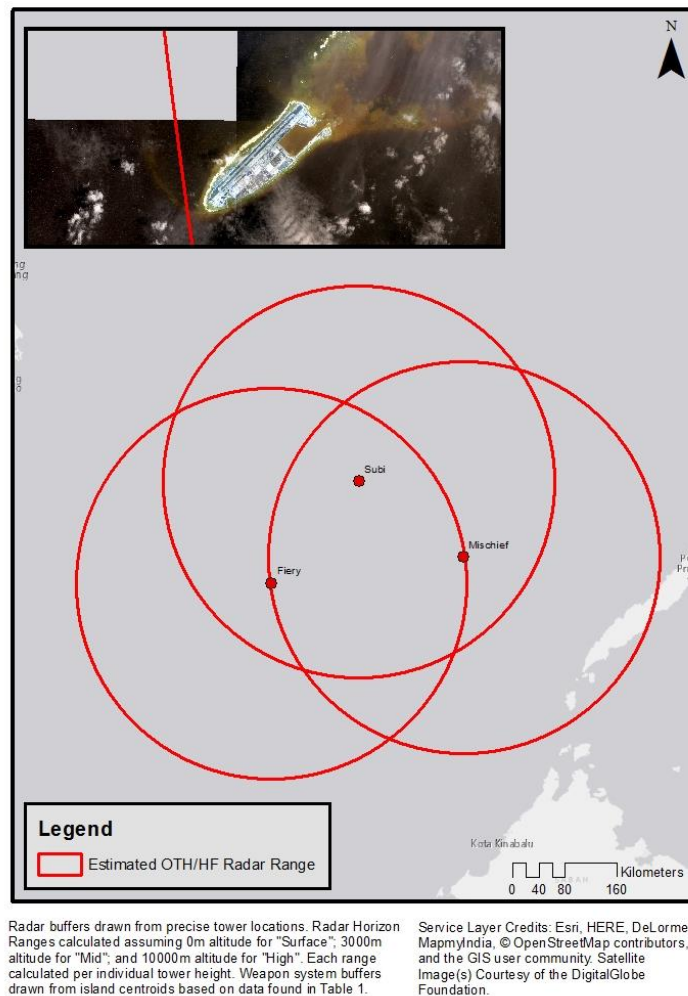

Figure 30: The Narrow Margins of OTH/HF Ranges with Fiery Cross Reef Inset

4.3. Range Corrections and Calculations

This thesis attempts to calculate the true radar horizons of radar towers identified on Fiery Cross, Mischief, and Subi Reefs in the SCS. In doing so, it provides a verifiable alternative to provided radar horizon ranges published by CSIS/AMTI. It is a useful case study of how the methodology discussed in Chapter 3 can be used to calculate and map radar horizons, but also of how the methodological processes can be used to reverse engineer existing data. It is unclear what CSIS/AMTI's estimate is limited by: radar horizon or radar strength. Radar systems can only detect objects if the power of the radar signal is strong enough to reach a distant target, bounce off that target, and return. CSIS/AMTI may well assume that the strength of signal emitted by radar systems in the SCS is only sufficient to reach their cited 50 km distance from the structures. However, there is no evidence either way to suggest a signal strength limitation, or lack there of. Therefore, this case study investigates CSIS/AMTI published ranges assuming no limitation to signal strength, in an ideal situation where the only limit is the radar horizon.

4.3.1. CSIS/AMTI Assumed Tower Height

It is worthwhile to compare the potential of a tower based on published estimates versus this study's calculations. In their estimation, CSIS/AMTI does not report what altitude their 50 km conventional radar range corresponds to; for the sake of this section, it is assumed that the estimate is not a limit of radar signal strength as discussed above. Therefore, a lack of announced altitude will equate to 0 m altitude. This 0m altitude at 50 km distance is significantly lower than the radar horizon of structures calculated in Section 4.1. Using Equation 5, the average height tower has a radar horizon at 40.41 m altitude at this same 50 km range.

*4.3.2. Adjusting for CSIS/AMTI Range Estimation*

It is nonetheless useful to evaluate the hypothetical implications of CSIS/AMTI's estimate. To determine how deviant this study's results are from the published estimates, the estimated range can be reverse-calculated to tell the necessary height of radar with such a radar horizon. Utilizing Equation 5, the height of a tower capable of observing an object at 0 m altitude within the radio spectrum at 50 km away is at minimum 147.28 m tall. This exceeds the average tower height measured in this study by 113.88 m. While this height is not inconceivable, nor is it uncommon for radar sensors to be placed on natural geographic features to achieve such heights, no buildings approaching this size were evident in the imagery. For all radar horizon ranges of a tower of this hypothetical height, see Table 6.

Table 6: Radar Horizons of CSIS/AMTI Assumed Tower Height

Minimum Required Height for CSIS/AMTI Est	Range at Surface Altitude (km)	Range at 3,000 m Altitude (km)	Range at 10,000 m Altitude (km)
147.28	50	275.66	461.10

4.3.3. Utilizing CSIS/AMTI Assumed Tower Heights

The coverages from Table 6 were visualized and plotted in the same manner as calculated radar horizon coverages from known precise radar tower locations (see Figure 31).
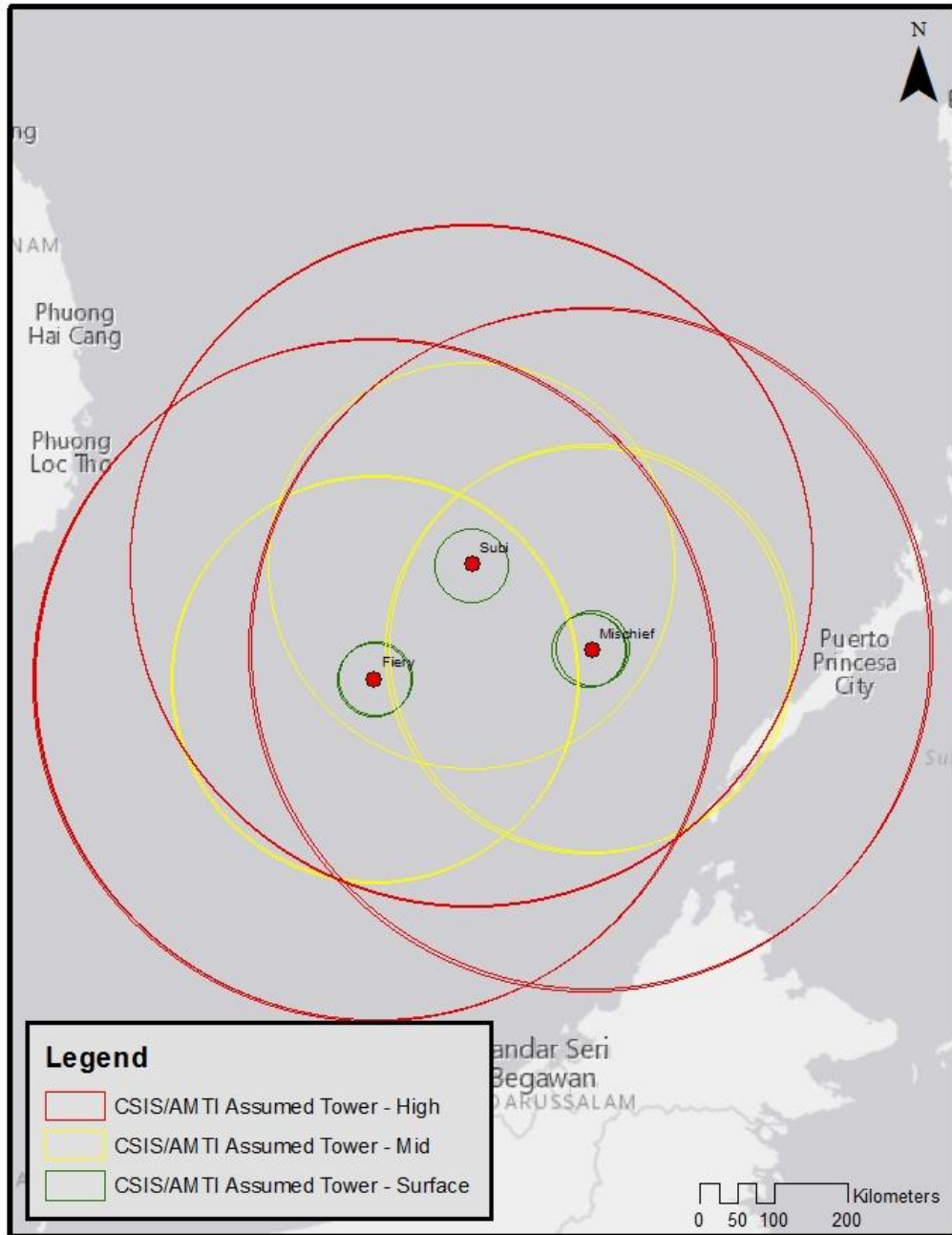
Radar buffers drawn from precise tower locations. Radar Horizon Ranges calculated assuming 0m altitude for "Surface"; 3000m altitude for "Mid"; and 10000m altitude for "High". Each range calculated per individual tower height. Weapon system buffers drawn from island centroids based on data found in Table 1.

Service Layer Credits: Esri, HERE, DeLorme, MapmyIndia, © OpenStreetMap contributors, and the GIS user community. Satellite Image(s) Courtesy of the DigitalGlobe Foundation.

Figure 31: Radar Horizons Calculated using CSIS/AMTI Assumed Tower Height

4.3.4. Final Coverage Differences

It is clear that the CSIS/AMTI estimate, and the hypothetical sensor locations required for its actualization, vary from ranges calculated by shadow-height analysis in this study. Ultimately, this variation in coverage was visualized by altitude category in Figures 32-34. It is important to evaluate these differences not only in distance but also area. The discrepancy in coverage between a single tower of necessary height to meet CSIS/AMTI's radar range estimate and that of a single tower of average height is therefore outlined in Table 7.

Likewise, the total observable area within each altitude category's radar horizon was calculated using the precise tower locations identified by study for the three focused islands. This data was derived from dissolved radar buffers, and the percent difference is reported in Table 8.

Table 7: Observable Area Differences Per Tower

	Area at Surface Altitude (km^2)	Area at 3,000 m Altitude (km^2)	Area at 10,000 m Altitude (km^2)
Average Calculated Height	1781.05	195520.8	596684.3
CSIS/AMTI Assumed Height	7853.98	238727.6	670554.1
Area for Average Calculated Height as Percentage of CSIS/AMTI Minimum Height	23 %	82 %	89 %
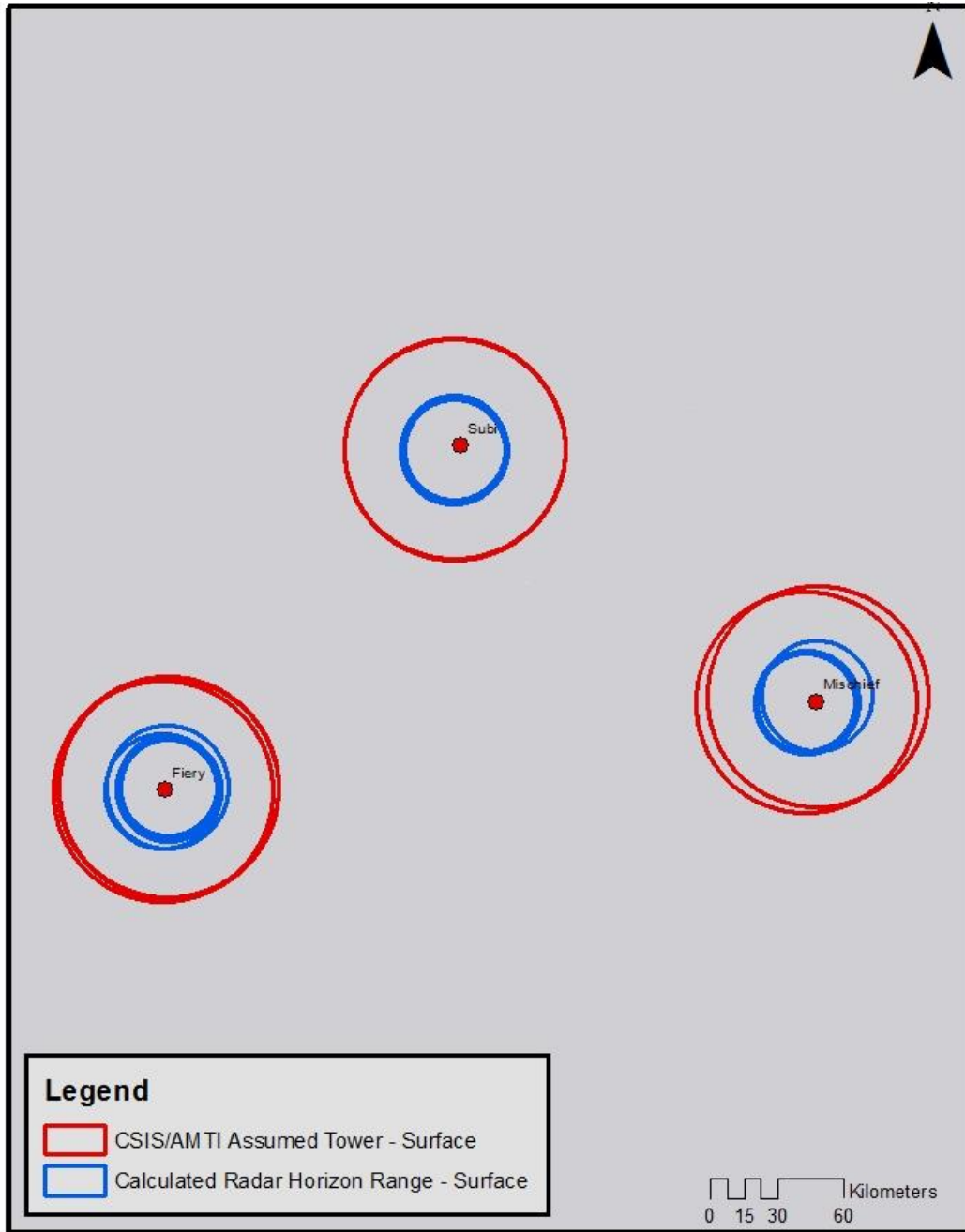
Radar buffers drawn from precise tower locations. Radar Horizon Ranges calculated assuming 0m altitude for "Surface"; 3000m altitude for "Mid"; and 10000m altitude for "High". Each range calculated per individual tower height. Weapon system buffers drawn from island centroids based on data found in Table 1.

Service Layer Credits: Esri, HERE, DeLorme, MapmyIndia, © OpenStreetMap contributors, and the GIS user community. Satellite Image(s) Courtesy of the DigitalGlobe Foundation.

Figure 32: Radar Horizon Range Discrepancy between Shadow Analysis Calculations and CSIS assumed height towers at Surface Altitude

Legend

CSIS/AMTI Assumed Tower - Mid

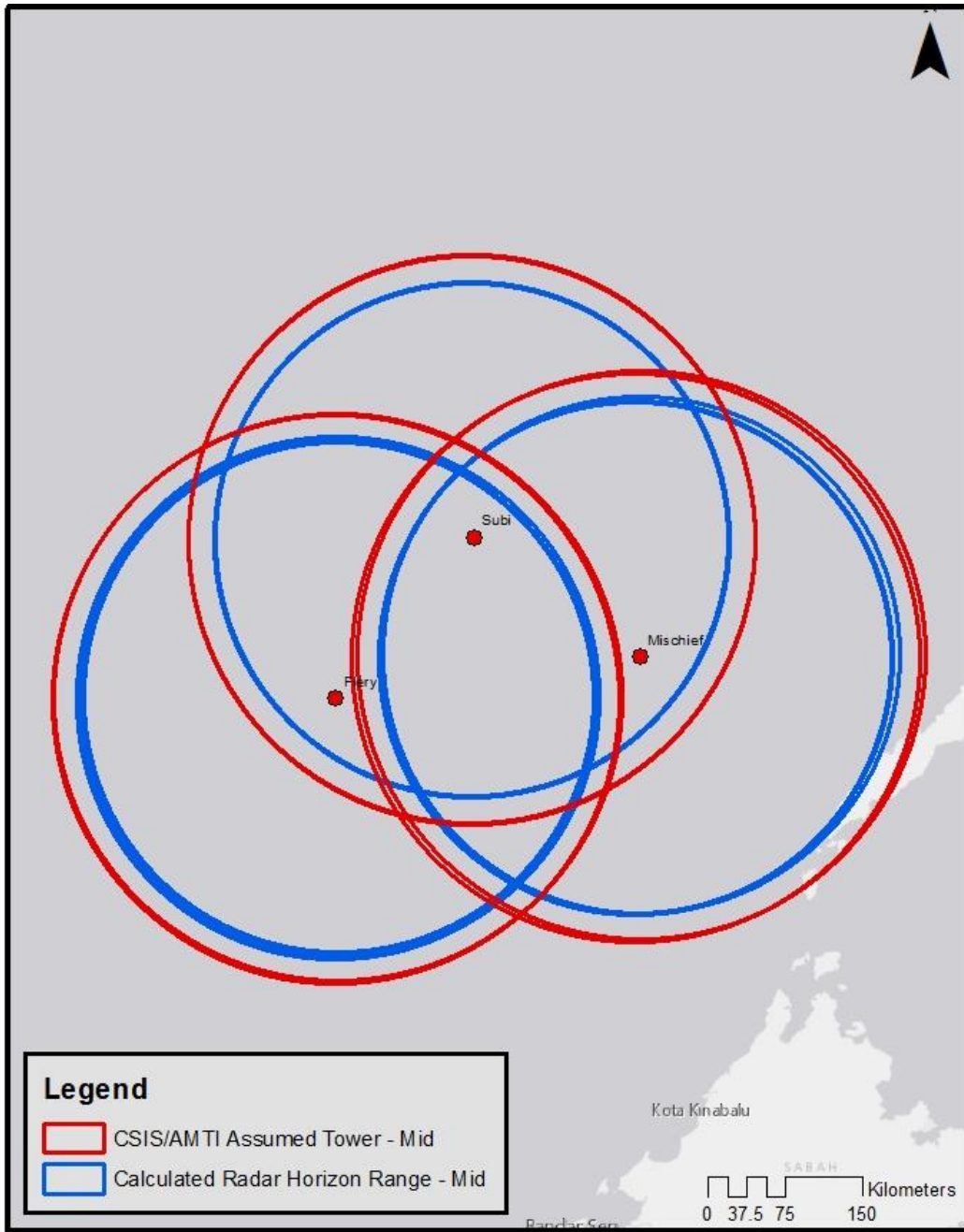Calculated Radar Horizon Range - Mid

Radar buffers drawn from precise tower locations. Radar Horizon Ranges calculated assuming 0m altitude for "Surface"; 3000m altitude for "Mid"; and 10000m altitude for "High". Each range calculated per individual tower height. Weapon system buffers drawn from island centroids based on data found in Table 1.

Service Layer Credits: Esri, HERE, DeLorme, MapmyIndia, © OpenStreetMap contributors, and the GIS user community. Satellite Image(s) Courtesy of the DigitalGlobe Foundation.

Figure 33: Radar Horizon Range Discrepancy between Shadow Analysis Calculations and CSIS assumed height towers at Mid Altitude
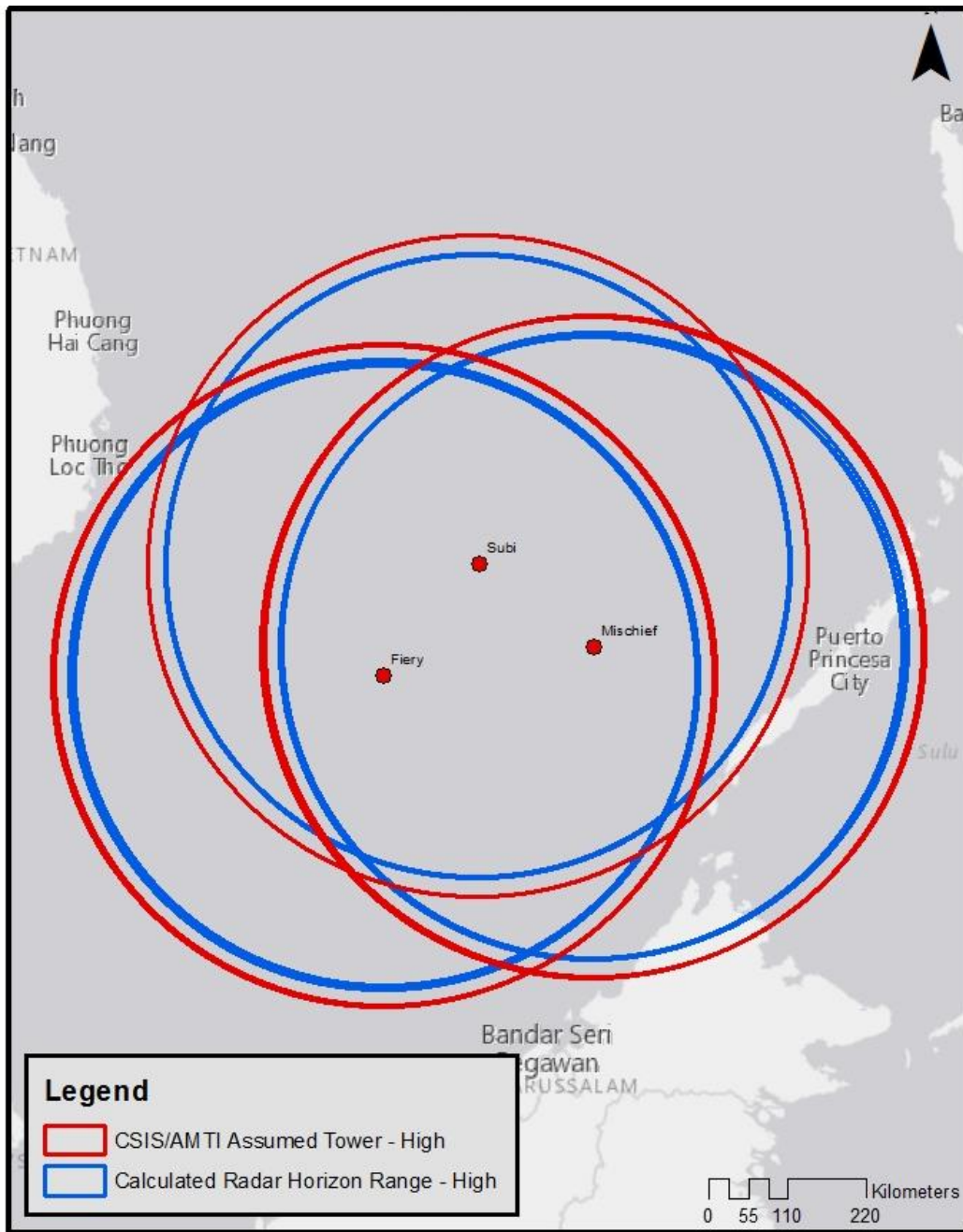
Figure 34: Radar Horizon Range Discrepancy between Shadow Analysis Calculations and CSIS assumed height towers at High Altitude

Table 8: Observable Area Differences From Tower Locations

	Total Area at Surface (km^2)	Total Area at 3,000m (km^2)	Total Area at 10,000m (km^2)
Average Calculated Height	6503190789.80	387274251358.84	924126470728.96
CSIS/AMTI Assumed Height	24561345968.31	446527333988.85	1012080290777.18
Total Area for Average Calculated Height as Percentage of CSIS/AMTI Minimum Height	26 %	87 %	91%

Chapter 5 Conclusions

This thesis was prepared to test the viability of using shadow photogrammetry in combination with radar propagation equations to map radar horizon ranges. The measurement of radar structure shadows allowed for radar horizon estimation, resulting in calculable radar ranges at various heights, as seen throughout the provided figures in Chapter 4 and the appendices. These measurements varied greatly from previous rule-of-thumb estimates provided by CSIS/AMTI and suggest a potentially more limited radar range than expected.

The results of the study prove the use of shadow photogrammetry and GIS as a radar range estimation method, giving detailed radar horizons for every radar tower. These ranges nonetheless display ideal conditions, and rest on multiple assumptions. In this regard, the study is limited by key factors, as well as the limited scope of this investigation. Inaccuracies originating from the study method itself, its limited scope, and lack of data resources may be overcome in future work.

5.1. Assessment of Methodology & Results

This study's methodology proved successful as a trial of integrated RS, GIS, and trigonometry as intended. The sheer volume of data provided by the DigitalGlobe Foundation – a problem that in itself is often a geospatial scientist's dream – proved a challenge for off-the-shelf GIS systems, and a variety of tools were necessary to filter data to an appropriately narrow scope. The use of mathematics and GIS data proved successful, as measurements were effectively integrated from RS sources, moved to conventional spreadsheet tools for calculation, and linked into a GIS for mapping and geographic calculations.

Radar horizon calculations made by this study varied substantially from CSIS/AMTI estimates. Radar horizons for measured towers on Fiery Cross, Mischief, and Subi Reefs at

average fell short of CSIS/AMTI range estimates by over 50% at surface altitude. Likewise, area coverage of calculated radar horizons was roughly 25% of the area expected by CSIS/AMTI estimates. Hypothetical situations in which CSIS/AMTI estimates could be made valid were modelled and compared to this study's calculated tower heights and radar horizons. These hypothetical scenarios are outlined in Section 4.3, which show that the overall deviation in range and area coverage of estimate to calculation decreased as range increased due to the negatively exponential nature of Earth's geometry curving away from the sensor.

The resulting radar horizon data indicates severe gaps in PRC radar coverage from structures on Fiery Cross, Mischief, and Subi Reefs. The limited range of surface horizons discussed in Section 4.1 allows for wide swathes of sea surface to remain out of conventional radar observation. These unobservable locations are also potentially below the minimum range of OTH/HF radar systems, increasing the vulnerability of these blind spots. The data suggests that conventional radar towers measured on the islands are not tall enough to provide sufficient coverage of the region at altitudes commensurate with other A2AD tools, as discussed in Section 4.2. Many tools' ranges exceed the coverage distances of conventional radar structures at appropriate altitudes. For example, while PRC anti-ship missiles may have enormous ranges, conventional radar would be inappropriate for targeting uses at such distance. This indicates a reliance on other targeting methods for such weapons. Likewise, the newest fighter aircraft available to the PRC is only covered by conventional ground-based radar at altitudes approaching its unloaded altitude ceiling (see Kable n.d.).

While there are other islands in the Spratly chain artificially created by the PRC, the three islands circumscribed by the Fiery Cross, Mischief, and Subi Reef constructions (Johnson Reef South, Hughes Reef, and Gavens Reefs) are not reported to house OTH/HF radar systems,

airfields, or extensive conventional radar arrays at the time of writing (CSIS/AMTI). These islands presently appear reliant on Fiery Cross, Mischief, and Subi Reef installations for many A2AD defenses. Therefore, the defensive capabilities, including the radar horizon ranges, of the "Big Three" reefs are vital to understanding A2AD defenses of the PRC's Spratly construction.

The study methodology initially planned to make use of GIS data provided by CSIS/AMTI. This could have potentially included analysis of any noted interior Spratly construction using average tower height data gathered from Fiery Cross, Mischief, and Subi Reefs. The poor data quality precluded this expansion.

5.2. Study Assumptions

There are multiple key assumptions made by the study which affect its scope and relevance. Namely, the study only investigates three of seven artificial PRC islands in the Spratly chain, though the biggest. It's investigation of radar coverage is also confined to conventional, ground-based radar systems, and cannot comment on the validity of OTH/HF ranges or the supplementation of ground-based systems with signals from aircraft or other methods of aerial surveillance. The methodology also relied greatly upon CSIS/AMTI reports for radar structure location and other details regarding the study topic. Though this study rejects conventional radar range estimates to create calculated radar horizons, it relies on similar estimates for other A2AD tools when comparing potential weapon system cooperation. While these estimates are even harder to correct, and likely impossible to calculate through a similar study, they represent a worthy topic of research.

5.3. Study Limitations and Sources of Inaccuracy

As this research effort set out to primarily create geospatial data in a data-poor environment, many of the geospatial and imagery inputs were of poor quality. GIS data from

CSIS/AMTI lacked key information required for this study rendering it largely irrelevant, while it could be argued that the methodology used in this study exceeded the validity of the DigitalGlobe Foundation's imagery GSDs. The vacuous data environment forced a methodology built around manual measurement, creating accuracy concerns. Manual tower height measurements, though rounded to reduce variability and establish a tighter control of measurement outcome, as well as manual centroid approximation, formed key – albeit questionable – data inputs.

This study, therefore, better proved the theory of its methodology rather than its exact structure. Automation of this methodology is necessary to remove confounding human variables. This would likely rely on an imagery classification system to find shadows, as used by Kwok (2014), Wegner (2014), or Miao (2016) combined with machine learning technology to correctly identify radar structures from the other, similar buildings. While this study did not need to measure shadow segments hidden behind radar structures due to fortuitous imagery angles, this methodology does not propose a solution to the issue. Additionally, shadows in this study were rarely spread over rough surfaces and were assumed to be spread across even surfaces. Solutions to these problems must be solved with image classification or inSAR as used by Wegner (2014), and the potential referencing of more advanced math and high-resolution DEM data.

5.4. Conclusions & Future Work

This study was performed to create geospatial data where current resources were lacking. Future research is needed to create this base data for analysis – much of this reliant upon the scarcity of even general, unstructured information from which GIS data can be created. The greatest takeaway from this study is the ability to create tailored geospatial data – in this case targeted toward radar horizon range estimation – in the limited data environment of foreign

defense analysis. The combination of RS, GIS, and trigonometry involved created defensible calculations for radar horizons, and offered alternative to previous, unproven radar range estimates. While the study relied on manual measurement and approximation, it provides a roadmap to future study and potential automation of similar efforts.

Future research may produce a wide variety of useful intelligence on PRC A2AD capabilities. While Chapter 2 discussed natural resources and lines of communication through the region, air defense identification zones (ADIZ) may be more appropriate for evaluation in conjunction with this project's data. At what altitudes Chinese radar can enforce an ADIZ is a potential topic of investigation. Further, the observational capabilities of OTH/HF radar and a more thorough understanding of radar blind spots should be studied, including models and visualizations with more direct utilization of the Z-axis.

This study's methodology can most directly be expanded to the study of other islands in the SCS, especially the remaining Spratly islands. To that end, the data of this project could be made far more applicable with inclusion of radar horizon limits from these islands. Construction on Johnson, Hughes, and Gavens Reefs may increase radar coverage within the circumscribed "Big Three" triangle by lowering the minimum radar horizon with more proximal radar structures, though they are not expected to greatly increase the observable area or reduce the minimum radar horizons for locations outside the Spratlys.

Improvement to this thesis is dependent upon time and resources. In the immediate term, this same study methodology could be applied to further sites in the SCS to calculate the radar horizons of other towers in the region that match similar description, as discussed above. These sites would likely come from identification in CSIS/AMTI figures, available through their web hosting. To expand the impact of the study, a more medium-term goal could be to integrate radar

horizon data from this study and any other known radar sites to examine the overlap of radar observation and natural resources in the region, territorial claims, or ADIZ boundaries, perhaps performing spatial analysis on the coverage dimensions between the two. To increase accuracy of measurement while maintaining manual control, multiple images could be used to make measurements with the results averaged. DEM data could also be added to get more accurate evaluation of surface heights to increase the accuracy of the current 1.6 m estimation discussed in Chapter 3. The shadow-height calculation strategy could be evaluated using ground-truthing against objects of similar size and shape to radar towers in an environment where knowledge of object size was available. Long-term, this study could benefit greatly from automation of measurements and calculations. Automation strategies could be adapted from Liasis & Stavrou (2016) or Wegner (2014), but for a data-scarce environment. Ultimately, the creation of a neural network for radar array identification within the imagery could be used to automate the entire methodology, with machine learning processes finding radar structures, automatically measuring their heights, calculating radar horizons based on these heights, and creating appropriate range buffers. This would likely look like an expansion of work by Kwok (2014) and Miao (2016) but adapted for object-oriented identification as seen in studies by Shimoni (2011) or McGlone (1994) and with a very different study focus. Eventually, this information could also be mapped in three dimensions, creating models similar to those of Kostic & Rancic (2003).

Cumulatively, this project effectively provided an initial stepping stone for verifiable radar range calculations in the SCS. This relied largely on imagery inputs, and only began the process of creating geospatial data for future research usage. Exploration on this frontier is necessary for a verifiable understanding of the PRC's A2AD capabilities in the SCS, and the fulfilment of US strategy goals.

References

Adeline, K.R.M., M. Chen, X. Briottet, S.k. Pang, and N. Paparoditis. "Shadow Detection in Very High Spatial Resolution Aerial Images: A Comparative Study." *ISPRS Journal of Photogrammetry and Remote Sensing* 80 (2013): 21-38. Web.

Al-Najdawi, Nijad, Helmut E. Bez, Jyoti Singhai, and Eran.a. Edirisinghe. "A Survey of Cast Shadow Detection Algorithms." *Pattern Recognition Letters* 33.6 (2012): 752-64. Web.

Alkanat, Ömer. "Determing the Surface-to-Air Missile Requirement for Western & Southern Part of the Turkish Air Defense System". MS Thesis (2008): n. pag. Air Force Institute of Technology - Wright-Patterson Air Force Base, Ohio. Department of the Air Force. Air University. Web. <http://www.dtic.mil/dtic/tr/fulltext/u2/a483275.pdf>.

AMTI. "Another Piece of the Puzzle." *Asia Maritime Transparency Initiative*, Center for Strategic and International Studies, 22 Feb. 2016, amti.csis.org/another-piece-of-the-puzzle/.

Ashdown, Neil. "What Is China's HQ-9 Air Defense System Capable of?" Edited by Gabriel Domínguez, *DW.COM*, Deutsche Welle, 17 Feb. 2016, www.dw.com/en/what-is-chinas-hq-9-air-defense-system-capable-of/a-19053690.

Bacon, David. "Chapter 14: Terrestrial Line-of-sight Links." *Propagation of Radiowaves*. 3rd ed. N.p.: IET, 2012. Http://dx.doi.org/10.1049/PBEW056E. Print

Bader, Jeffrey A. "The U.S. and China's Nine-Dash Line: Ending the Ambiguity." Brookings, Brookings, 28 July 2016, www.brookings.edu/opinions/the-u-s-and-chinas-nine-dash-line-ending-the-ambiguity/.

Bell, John E., Stanley E. Griffis, William A. Cunningham, and Jon A. Eberlan. "Location Optimization of Strategic Alert Sites for Homeland Defense." *Omega* 39.2 (2011): 151-58. Web.

Booker, H.g. "Elements of Radio Meteorology: How Weather and Climate Cause Unorthodox Radar Vision beyond the Geometrical Horizon." *Journal of the Institution of Electrical Engineers - Part IIIA: Radiolocation*, vol. 93, no. 1, 1946, pp. 69–78., doi:10.1049/ji-3a-1.1946.0025.

Brainware, LLC. "Tide Predictions for Any Location in the World." *WorldTides*, University of Oregon, www.worldtides.info/.

Brown, Peter J. "Calculated Ambiguity in the South China Sea." *Asia Times Online*. N.p., 8
Dec. 2009. Web.

Buszynski, Leszek. "The South China Sea: Oil, Maritime Claims, and U.S.-China Strategic
Rivalry." *The Washington Quarterly* 35.2 (2012): 139-56. Web.

Cheng, Dean. "The U.S. Needs an Integrated Approach to Counter China's Anti-Access/Area
Denial Strategy." The Heritage Foundation. N.p., 9 July 2014. Web. 09 Apr. 2017.

Cheng-yi Lin, "Taiwan's South China Sea Policy," Asian Survey, Vol. 37 (1997): 323– 324

China Power Team. "How much trade transits the South China Sea?" China Power. August 2,
2017. Updated September 12, 2017. Accessed October 22, 2017.
https://chinapower.csis.org/much-trade-transits-south-china-sea/

Cooper, Cortez. "Podcast: China's New Spratly Island Defenses, with Michael McDevitt and
Cortez Cooper." *China's New Spratly Island Defenses, with Michael McDevitt and
Cortez Cooper*, Center for Strategic and International Studies, Jan. 2017,
soundcloud.com/csis-57169780/chinas-new-spratly-island-defenses.

Cordova, Henry. "Elevation Determination By Shadow Measurement From Vertical
Monoscopic Aerial Imagery." Pecora 16 "Global Priorities in Land Remote Sensing", 23
Oct. 2005, www.asprs.org/a/publications/proceedings/pecora16/Cordova_H.pdf.

Cornwall, Chris, et al. "NOAA Solar Position Calculator." Earth System Research Laboratory,
National Oceanic & Atmospheric Administration,
www.esrl.noaa.gov/gmd/grad/solcalc/azel.html.

Davin, Matthew E. "Anti-Access/Area Denial: Time To Ditch the Bumper Sticker?" *Joint
Military Operations Department* (2013): n. pag. Web.

EIA. "South China Sea Analysis." U.S. Energy Information Administration - EIA - Independent
Statistics and Analysis, 7 Feb. 2013. Web.

Evers, Hans-Dieter. "Reframing the South China Sea - Towards a Mediterranean Understanding
of Culture and Resources." *Conceptions of Maritime Space: A Cultural Perspective on
the South China Sea* (2013): n. pag. Web.

Franklin, Randolp, Clark Ray, and Shashank Mehta. *Geometric Algorithms for Siting of Air
Defense Missile Batteries*. *Battelle, Columbus Division*. Department of the Army, 1994.
n.d. Web.

Gallagher, Michael G. "China's Illusory Threat to the South China Sea." *International Security* 19.1 (1994): 169. Web.

Gao, Zhigao, and Bing Bing Jia. "The Nine-Dash Line in The South China Sea: History, Status, and Implications." *The American Journal of International Law* 107.1 (2013): 98-124. Web.

Gerson, Michael, and Alison Lawler Russell. "Conference Report." *American Grand Strategy & Seapower* (2011): n. pag. *Https://www.cna.org/*. Center for Naval Analyses, 4 Aug. 2011. Web. Nov. 2011.

Gonsalves, Paul, Janet Burge, and Ben Popp. "Decision Support System for Theater Missile Defense." *Signal Processing, Sensor Fusion, and Target Recognition* 5096.XII (2003): n. pag. Web. 21 Apr. 2003.

Gormley, Dennis M, et al. "A Potent Vector: Assessing Chinese Cruise Missile Developments." National Defense University Press, Joint Force Quarterly 75, 30 Sept. 2014, ndupress.ndu.edu/Media/News/News-Article-View/Article/577568/jfq-75-a-potent-vector-assessing-chinese-cruise-missile-developments/.

Gungwu, Wang. "THE NANHAI TRADE: A Study of the Early History of Chinese Trade in the South China Sea." *Journal of the Malayan Branch of the Royal Asiatic Society* (182) 31.2 (1958): 3-135. Web.

Guo, Jianhong, et al. "Removing Shadows from Google Earth Images." *International Journal of Remote Sensing*, vol. 31, no. 6, 30 Mar. 2010, pp. 1379–1389., doi: http://dx.doi.org/10.1080/01431160903475316.

Haslett, Christopher. "Essentials of radio wave propagation". Cambridge University Press, p. 119–120, 2008. Web.

Hayton, Bill. "China's 'Historic Rights' in the South China Sea: Made in America?" The Diplomat, The Diplomat, 22 June 2016, thediplomat.com/2016/06/chinas-historic-rights-in-the-south-china-sea-made-in-america/.

Hooker, R.D. "The Grand Strategy of the United States." *INSS Strategic Monograph* (n.d.): n. pag. National Defense University Press, Oct. 2014. Web.

Hoyler, Marshall. "An unpersuasive argument for overcoming China's A2AD capability." Naval War College Review, Autumn 2013, p. 135+. Academic OneFile, Accessed 22 Oct. 2017.

Kable Intelligence. "J-10 (Jian 10) Vigorous Dragon Multirole Tactical Fighter." *Airforce Technology*, Kable Intelligence Limited, www.airforce-technology.com/projects/j-10/.

Kaplan, Robert D. "Chapter 2: China's Caribbean." *Asia's Cauldron: The South China Sea and the End of a Stable Pacific*. N.p.: Random House USA, 2015. N. pag. Print.

Kostic, A., and D. Rancic. "Radar Coverage Analysis in Virtual GIS Environment." *6th International Conference on Telecommunications in Modern Satellite, Cable and Broadcasting Service, 2003. TELSIKS 2003.* (n.d.): n. pag. Web.

Krepinevich, Andrew, Barry Watts, and Robert Work. *Meeting the Anti-Access and Area-Denial Challenge*. Publication. Washington, D.C.: Center for Strategic and Budgetary Assessments, 2003. *Csbaonline.org*. Web.

Kucera, Paul A., Witold F. Krajewski, and C. Bryan Young. "Radar Beam Occultation Studies Using GIS and DEM Technology: An Example Study of Guam." *Journal of Atmospheric and Oceanic Technology* 21.7 (2004): 995-1006. Web.

Kwatra, M.H.V., and S. Dai, "Shadow Removal for Aerial Imagery by Information Theoretic Intrinsic Image Analysis", *Proc. IEEE Int'l Conf. Computational Photography*, 2012

Kwok, R. "Declassified high-resolution visible imagery for Arctic sea ice investigations: An overview," *Remote Sens. Environ.*, vol. 142, pp. 44–56, Feb. 2014.

Larson, R. E., R. P. Hostetler, and B. H. Edwards. 1993. *Precalculus: A Graphing Approach*. D. C. Heath and Company, Lexington, MA.

Lee, Victor Robert. "South China Sea: Satellite Imagery Shows China's Buildup on Fiery Cross Reef." The Diplomat, The Diplomat, 16 Sept. 2015, thediplomat.com/2015/09/south-china-sea-satellite-imagery-shows-chinas-buildup-on-fiery-cross-reef/.

Li, Jinming, and Dexia Li. "The Dotted Line on the Chinese Map of the South China Sea: A Note." *Ocean Development & International Law* 34.3-4 (2003): 287-95. Web.

Li, Y., Gong, P., Sasagawa, T., 2005. "Integrated shadow removal based on photogrammetry and image analysis." *Int. J. Rem. Sens.* 26 (18), 3911–3929.

Liasis, Gregoris, and Stavros Stavrou. "Satellite Images Analysis for Shadow Detection and Building Height Estimation." *ISPRS Journal of Photogrammetry and Remote Sensing* 119 (2016): 437-50. Web.

Liu, Nan, Bo Huang, and Magesh Chandramouli. "Optimal Siting of Fire Stations Using GIS and ANT Algorithm." *Journal of Computing in Civil Engineering* 20.5 (2006): 361-69. Web.

McCarthy, Christopher J. "Anti-Access/Area Denial: The Evolution of Modern Warfare." *Lucent*. U.S. Naval War College, 2010. Web.

McDevitt, Mike. "Podcast: China's New Spratly Island Defenses, with Michael McDevitt and Cortez Cooper." *China's New Spratly Island Defenses, with Michael McDevitt and Cortez Cooper*, Center for Strategic and International Studies, Jan. 2017, soundcloud.com/csis-57169780/chinas-new-spratly-island-defenses.

McDougall, Walter A. "Can the United States Do Grand Strategy?" *The Telegram*. Foreign Policy Research Institute, 13 Apr. 2010. Web. 09 Apr. 2017.

McGlone, J. Chris, and Jefferey A. Shufelt. "Projective and Object Space Geometry For Monocular Building Extraction." *IEEE Conference on Computer Vision and Pattern Recognition*, 2 Mar. 1994. *Carnegie-Mellon University of Pittsburgh, PA*, Department of Computer Science, http://www.dtic.mil/get-tr-doc/pdf?AD=ADA277586.

Miao, Xin, Hongjie Xie, Stephen F. Ackley, and Songfeng Zheng. "Object-Based Arctic Sea Ice Ridge Detection From High-Spatial-Resolution Imagery." *Geoscience and Remote Sensing Letters* 13.6 (2016): 787-91. Web.

Nagao, M., Matsuyama, T., Ikeda, Y., 1979. "Region extraction and shape analysis in aerial photographs." *Comput. Graph. Image Process*. 10 (3), 195–223.

Nathanson, Fred E, et al. *Radar Design Principles: Signal Processing and the Environment*. 2nd ed., McGraw-Hill, 1991, selasl.files.wordpress.com/2011/08/mcgraw_hill_-_radar_design_principles.pdf.

NAVAIR. "Chp 4: Radar Horizon / Line of Sight." *Electronic Warfare and Radar Systems Engineering Handbook*, United States Naval Air Systems Command, U.S. Navy's Weapons Division Avionics Department Electronic Warfare Division, 2013.

O'Mara, Patrick R., LCDR, USN. "History's Role in Operational Design and Planning: How Germany's Failed Invasion Provides Insight into US and Chinese Perspectives on A2AD." *USMC Command and Staff College* (2013): n. pag. Web.

Overcash, David M. "Through the Lens of Operational Art: Countering People's Republic of China (PRC) Aggression in a Limited Conflict Using Innovative Ways and Cost-

Effective Means to Offset PRC Anti-Access Area Denial (A2AD) Capabilities. How Should Pacific Command's (PACOM) Theater Campaign Plan Evolve in Light of the Center for Strategic and Budgetary Assessment's (CSBA) Recent AirSea Battle Concept (ASBC) Proposal?" Defense Technical Information Center, http://www.dtic.mil/dtic/tr/fulltext/u2/a535576.pdf.

Page, Jeremy. "Tribunal Rejects Beijing's Claims to South China Sea." The Wall Street Journal, Dow Jones & Company, 12 July 2016, www.wsj.com/articles/chinas-claim-to-most-of-south-china-sea-has-no-legal-basis-court-says-1468315137.

PDCC - Republic of China (Taiwan). Ministry of Foreign Affairs. Public Diplomacy Coordination Council. *Statement on the South China Sea*. By PDCC. N.p., 7 July 2015. Web.

Plait, Phil. "How Far Away Is the Horizon?" Discover Magazine, 15 Jan. 2009, blogs.discovermagazine.com/badastronomy/2009/01/15/how-far-away-is-the-horizon/#.WiKAiEqWZPY.

Raju, P. L. N., et al. "Shadow Analysis Technique for Extraction of Building Height Using High Resolution Satellite Single Image and Accuracy Assessment." ISPRS - International Archives of the Photogrammetry, Remote Sensing and Spatial Information Sciences, XL-8, 2014, pp. 1185–1192., doi:10.5194/isprsarchives-xl-8-1185-2014.

Richardson, John. "Deconstructing A2AD." *The National Interest*. The Center for the National Interest, 3 Oct. 2016. Web. 09 Apr. 2017.

Rogers, T., L. Ames, and E. Martin. "The Possibity of Extending Air-Ground UHF Voice Communications to Distances Far Beyond the Radio Horizon." *IEEE Transactions on Communications* 5.1 (1957): 106-21. Web.

Shao, Yang, Gregory N. Taff, and Stephen J. Walsh. "Shadow Detection and Building-height Estimation Using IKONOS Data." *International Journal of Remote Sensing* 32.22 (2011): 6929-944. Web.

Shimoni, M., Tolt, G., Perneel, C., Ahlberg, J., 2011. "Detection of vehicles in shadow areas." *Proc. 3rd Workshop on Hyperspectral Image and Signal Processing: Evolution in Remote Sensing*, WHISPERS, 6–9 June, Lisbon, Portugal, pp. 1–4.

Skolnik, Merrill I. "Chapter 1: An Introduction to Radar." *Introduction to Radar Systems*. N.p.: McGraw-Hill, 2007. N. pag. Print.

Sofaer, Abraham D. "The Philippine Law of the Sea Action against China: Relearning the Limits of International Adjudication." *Chinese Journal of International Law* (2016): n. pag. Web.

Souza, George Bryan. *The Survival of Empire: Portuguese Trade and Society in China and the South China Sea, 1630-1754*. N.p.: Cambridge UP, 2004. Print.

Straitiff, Stephanie L., and Robert G. Cromley. "Using GIS and K = 3 Central Place Lattices for Efficient Solutions to the Location Set-Covering Problem in a Bounded Plane." *Transactions in GIS* 14.3 (2010): 331-49. *Wiley Online Library*. Web.

Tsuruoka, Doug. "Undersea Cables the Achilles' Heel in Lead-up to New Cold War." Asia Times. NCIS Counter Intelligence Newletter, 6 Jan. 2018, www.atimes.com/article/undersea-cables-achilles-heel-lead-new-cold-war/.

Valtr, Pavel, and Pavel Pechac. "The Influence of Horizontally Variable Refractive Index Height Profile on Radio Horizon Range." *Antennas & Wireless Propagation Letters* 4 (2005): 489-91. Web.

Wang, Kuan-Hsiung. "The ROC's Maritime Claims and Practices with Special Reference to the South China Sea." *Ocean Development & International Law* 41.3 (2010): 237-52. Web.

Wegner, Jan Dirk, Jens R. Ziehn, and Uwe Soergel. "Combining High-Resolution Optical and InSAR Features for Height Estimation of Buildings With Flat Roofs." *IEEE Transactions on Geoscience and Remote Sensing* 52.9 (2014): 5840-854. Web

Yanagi, Tetsuo, et al. "Co-Tidal and Co-Range Charts in the South China Sea Derived from Satellite Altimetry Data." La Mer, Societe Franco-Japonaise D'Oceanographie, vol. 35, 1997, pp. 85–93., www.sfjo-lamer.org/la_mer/35-3/35-3-1.pdf.

Zemmari, Reda, Martina Daun, and Ulrich Nickel. "Maritime Surveillance Using GSM Passive Radar." *19th International Radar Symposium* (2012): n. pag. Web.

Zhao, Guocai. "Analysis of the Sovereign Dispute over the Spratlys under the Present Law of Sea", Asian Review, Vol. 9, (Hong Kong, 1999): 22

Appendix A: Data Notes

Relevant Imagery Metadata

Mischief Reef

 Source: WV04 2017-12-27
 Image ID: 9929b355-14fa-42e7-8408-41338ef178d9-inv
 Image Clouds: 5.9%
 Image Nadir: 16.3°
 Bands: 4-BANDS
 Max GSD (panchromatic; multispectral): 0.33m; 1.24m
 Sun Elevation: 50.7°
 Max Target Azimuth: 97.3°

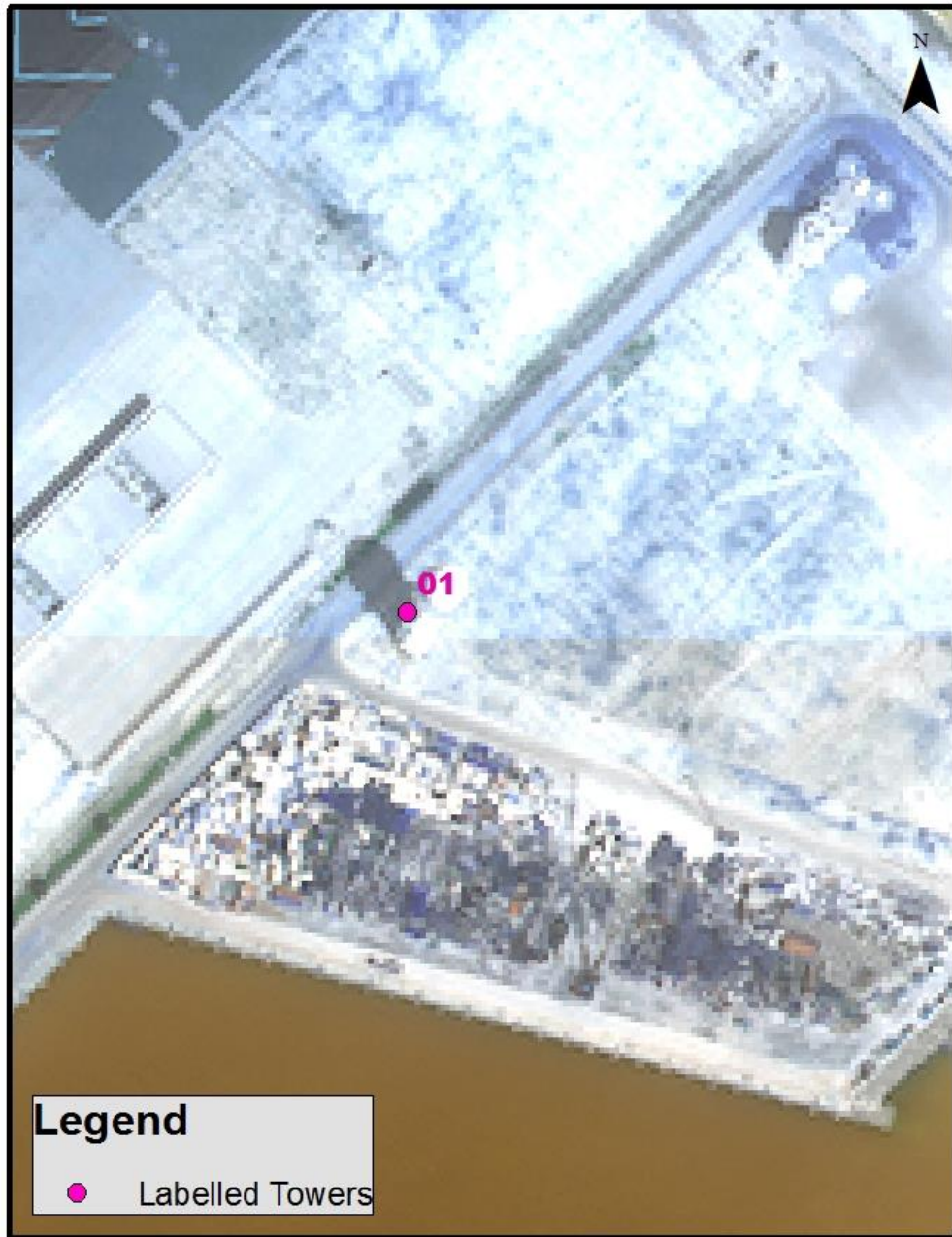Fiery Cross Reef

 Source: GE01 2018-01-01
 Image ID: 105001000D959600
 Image Clouds: 18.0%
 Image Nadir: 26.7°
 Bands: 4-BANDS
 Max GSD (panchromatic; multispectral): 0.51m; 1.84m
 Sun Elevation: 51.7°
 Max Target Azimuth: 35.3

Subi Reef

 Source: WV03 2017-12-07
 Image ID: 10400100355E1900
 Image Clouds: 13.0%
 Image Nadir: 21.6°
 Bands: 8-BANDS
 Max GSD (panchromatic; multispectral): 0.35m; 1.24m
 Sun Elevation: 53.6°
 Max Target Azimuth: 220.6

Manually Created Approximate Visual Centroid Locations

Island Center	Lat (m)	Long (m)
Mischief	12,861,812.43	1,107,671.14
Subi	12,700,467.05	1,223,722.42
Fiery Cross	12,566,668.92	1,067,786.09

Appendix B: Labelled Imagery of Identified Radar Zones

Radar Zone FC1 - Fiery Cross Reef

N

01

Legend

● Labelled Towers

0   40   80   160   Meters

Service Layer Credits: Esri, HERE, DeLorme, MapmyIndia, © OpenStreetMap contributors, and the GIS user community. Satellite Image(s) Courtesy of the DigitalGlobe Foundation.
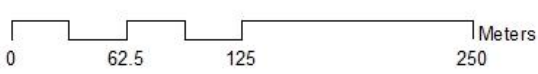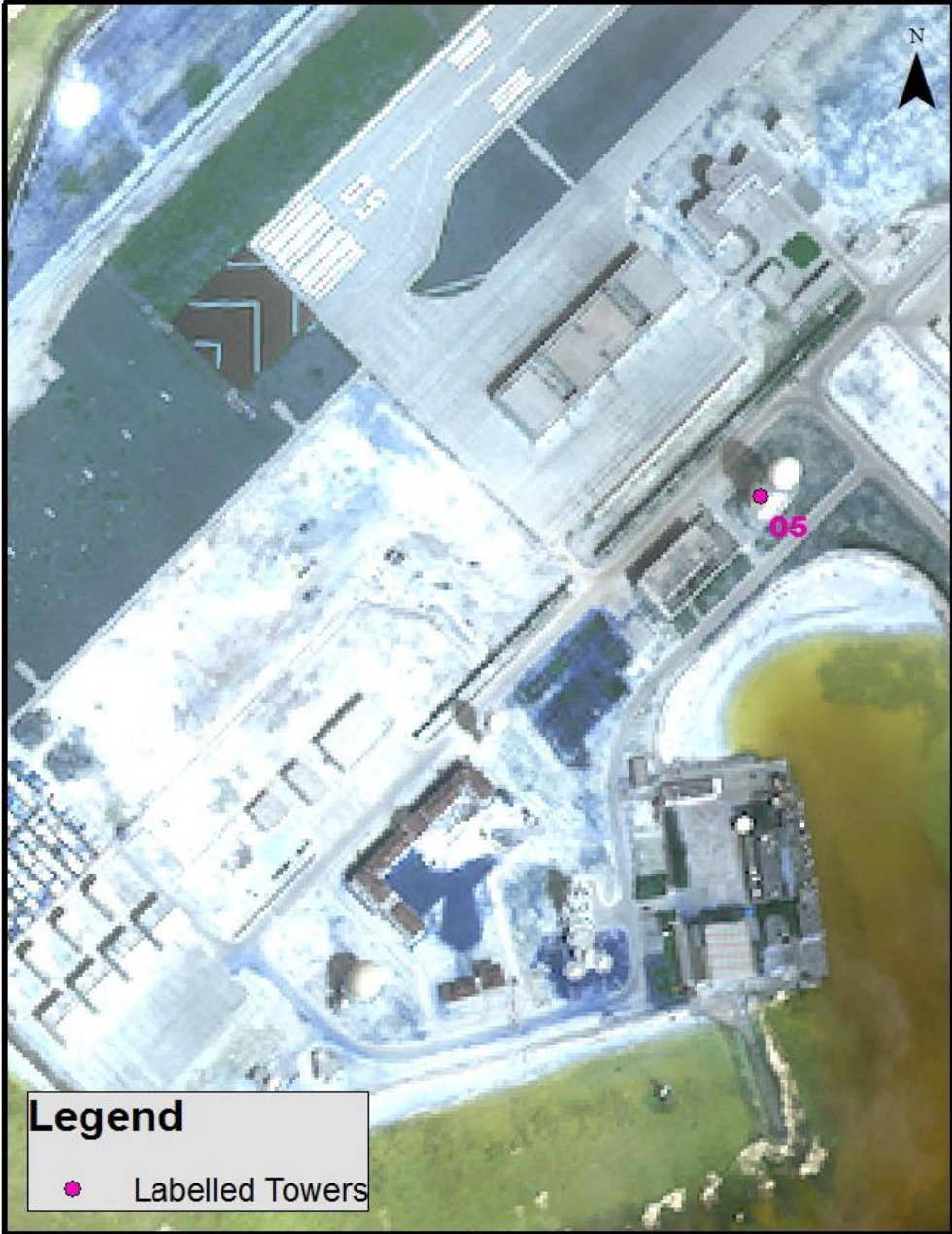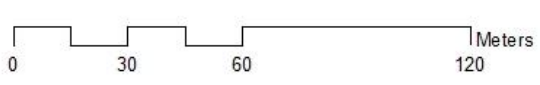
Radar Zone FC2 - Fiery Cross Reef

Legend

• Labelled Towers

0   40   80   160   Meters

Service Layer Credits: Esri, HERE, DeLorme,
MapmyIndia, © OpenStreetMap contributors,
and the GIS user community. Satellite
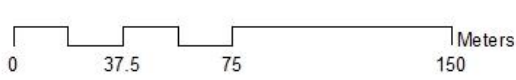Image(s) Courtesy of the DigitalGlobe
Foundation.

Radar Zone FC3 - Fiery Cross Reef

N

Legend

● Labelled Towers

0 62.5 125 250 Meters

Service Layer Credits: Esri, HERE, DeLorme, MapmyIndia, © OpenStreetMap contributors, and the GIS user community. Satellite Image(s) Courtesy of the DigitalGlobe Foundation.

Radar Zone S1 - Subi Reef
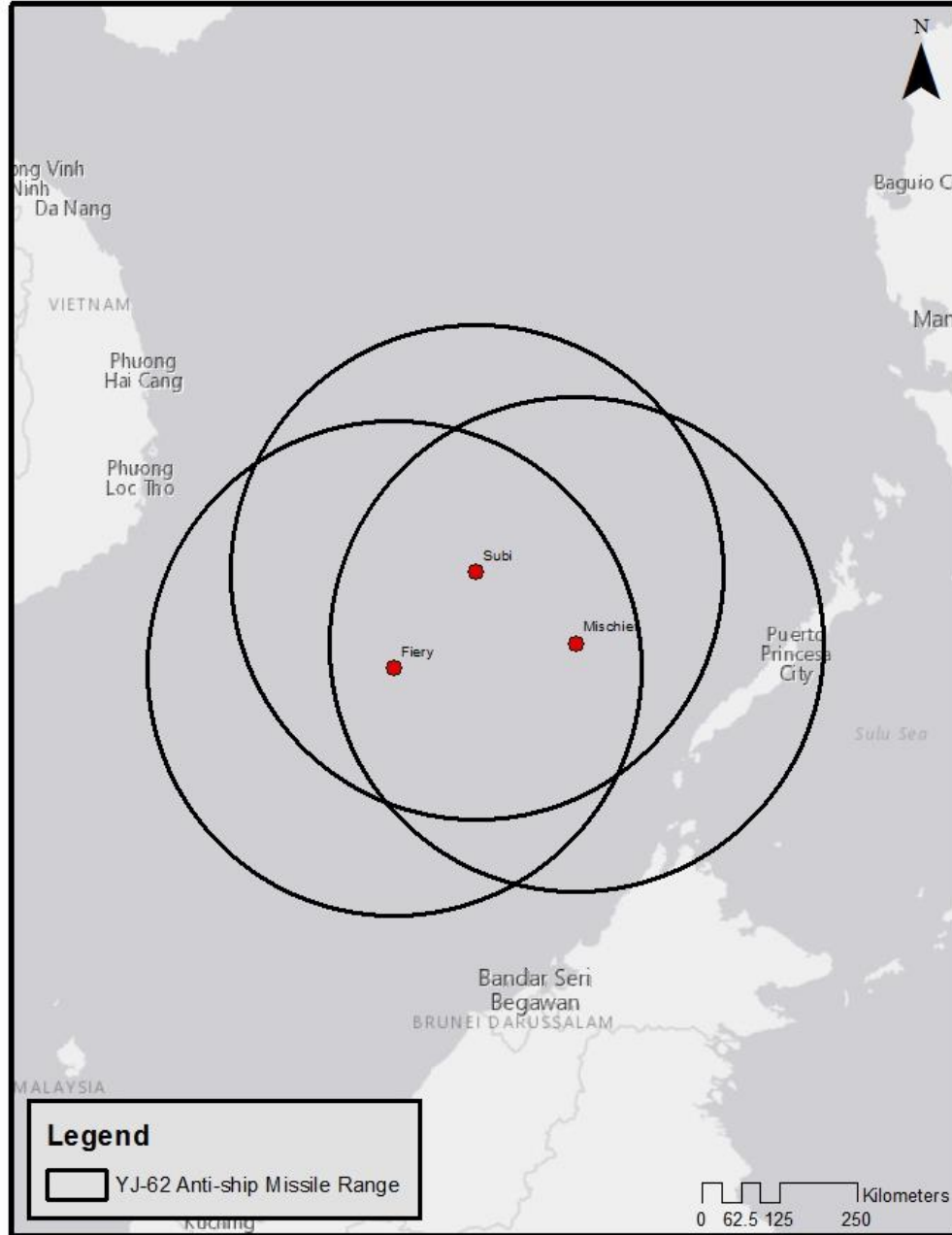

N

10

Legend

● Labelled Towers

0   30   60   120 Meters

Service Layer Credits: Esri, HERE, DeLorme,
MapmyIndia, © OpenStreetMap contributors,
and the GIS user community. Satellite
Image(s) Courtesy of the DigitalGlobe
Foundation.

Radar Zone S2 - Subi Reef

Legend

● Labelled Towers

Meters
0   30   60   120

Radar Zone M1 - Mischief Reef

Legend

● Labelled Towers

0   37.5   75   150   Meters

Service Layer Credits: Esri, HERE, DeLorme,
MapmyIndia, © OpenStreetMap contributors,
and the GIS user community. Satellite
Image(s) Courtesy of the DigitalGlobe
Foundation.

Radar Zone M2 - Mischief Reef

Legend

● Labelled Towers

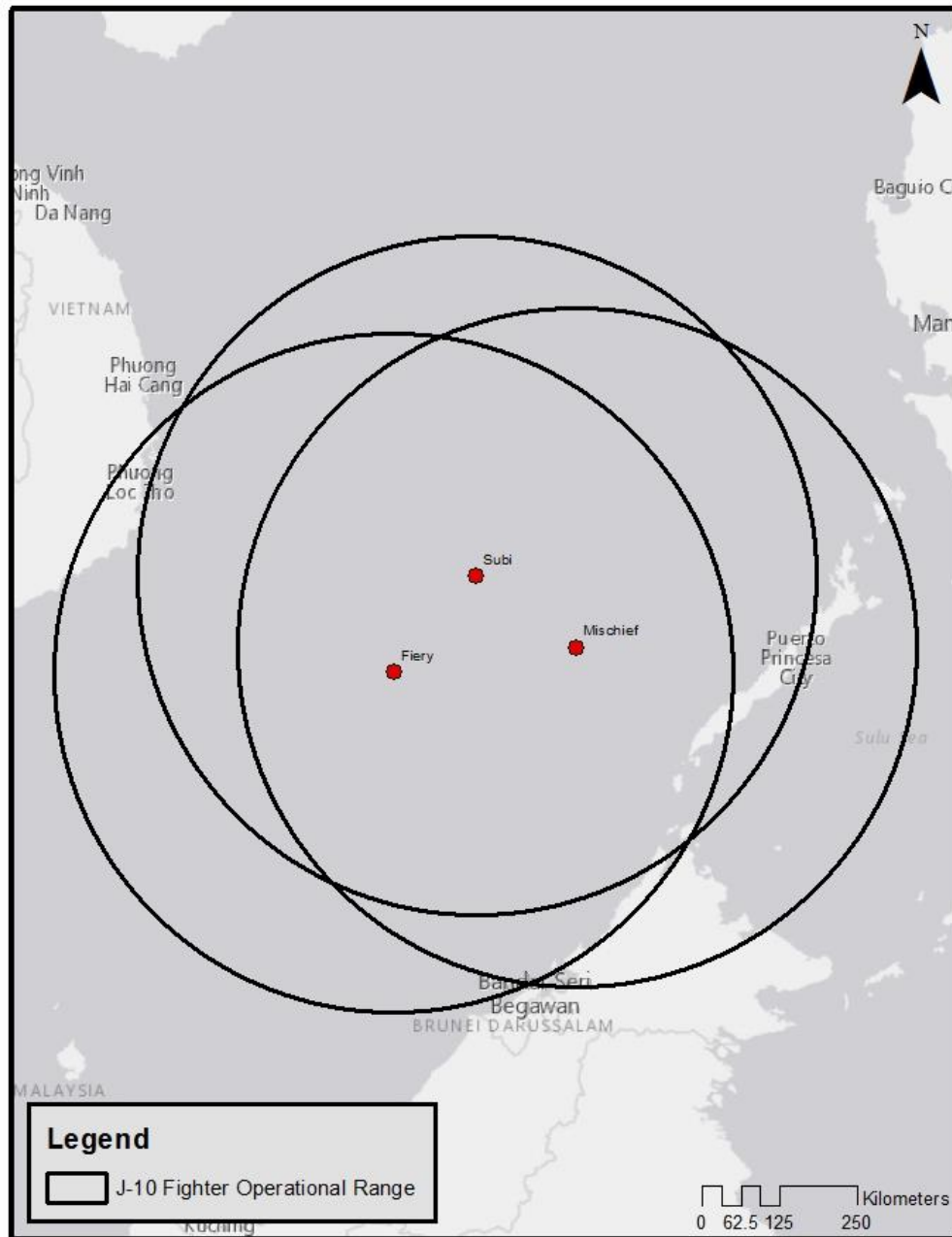0   50   100   200 Meters

Appendix C: Weapon System Ranges

YJ-62 ASM Range

Radar buffers drawn from precise tower locations. Radar Horizon Ranges calculated assuming 0m altitude for "Surface"; 3000m altitude for "Mid"; and 10000m altitude for "High". Each range calculated per individual tower height. Weapon system buffers drawn from island centroids based on data found in Table 1.

Service Layer Credits: Esri, HERE, DeLorme, MapmyIndia, © OpenStreetMap contributors, and the GIS user community. Satellite Image(s) Courtesy of the DigitalGlobe Foundation.
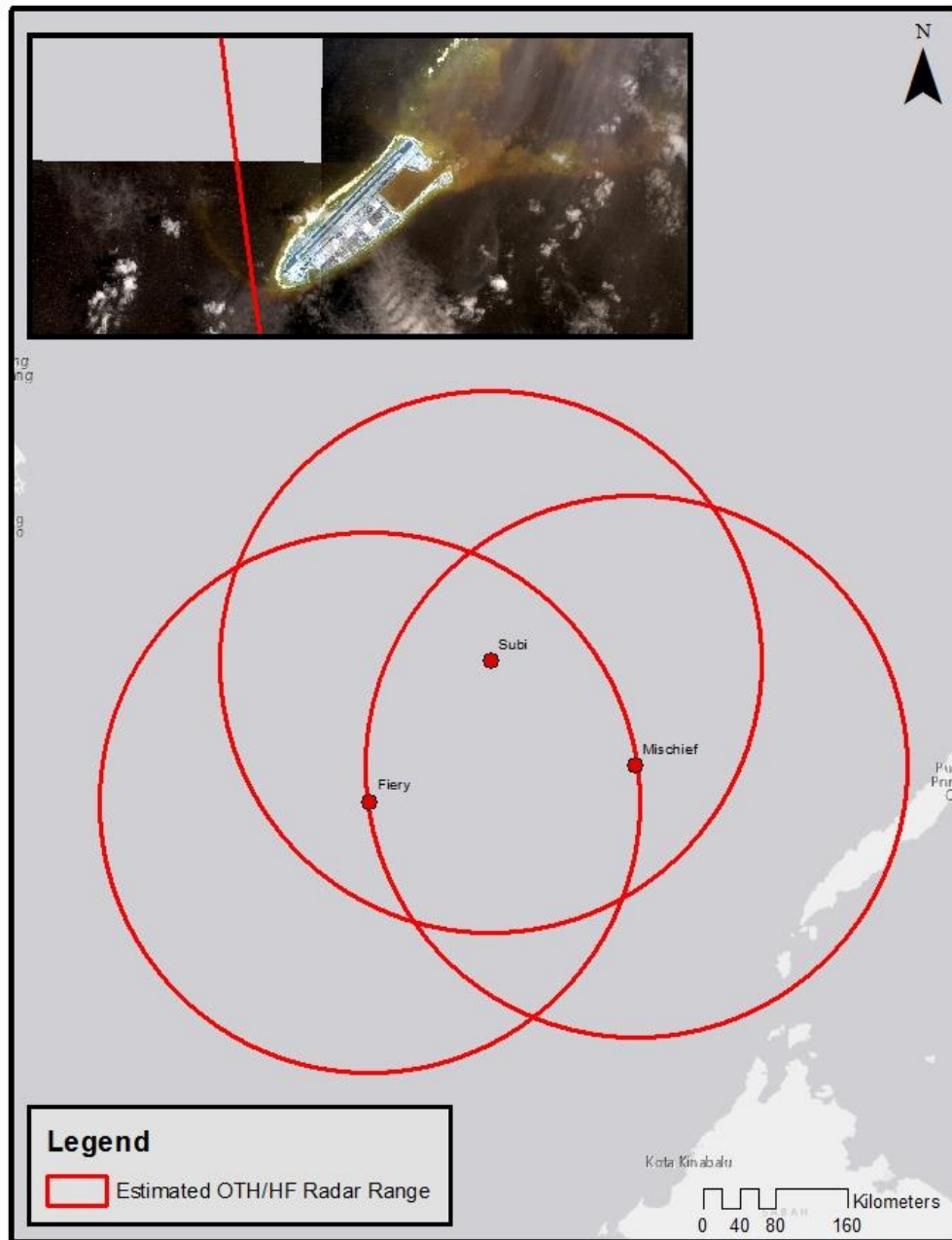
J-10 Fighter Operational Range

Radar buffers drawn from precise tower locations. Radar Horizon Ranges calculated assuming 0m altitude for "Surface"; 3000m altitude for "Mid"; and 10000m altitude for "High". Each range calculated per individual tower height. Weapon system buffers drawn from island centroids based on data found in Table 1.

Service Layer Credits: Esri, HERE, DeLorme, MapmyIndia, © OpenStreetMap contributors, and the GIS user community. Satellite Image(s) Courtesy of the DigitalGlobe Foundation.
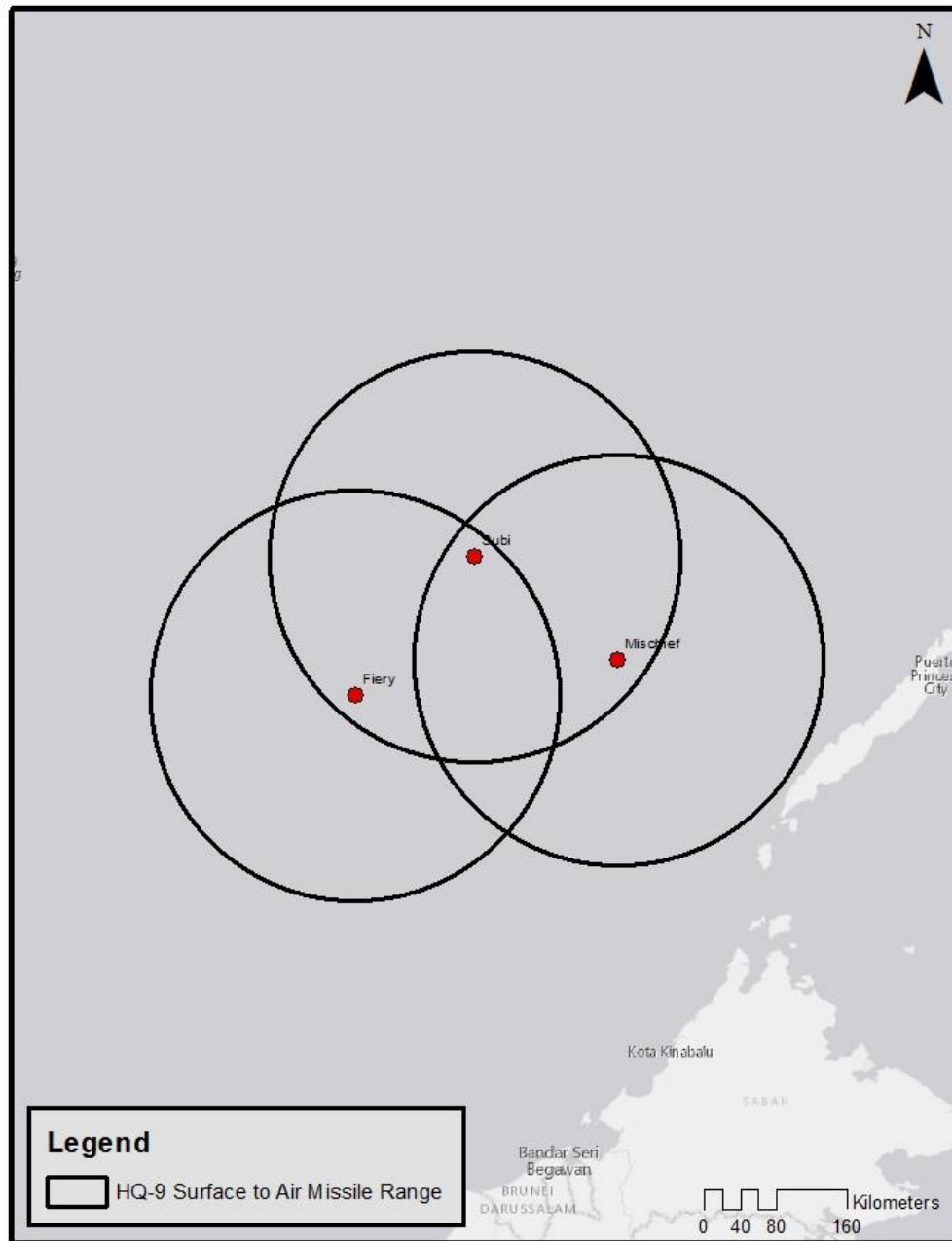
OTH/HF Range Estimate with Fiery Cross Reef Inset

Legend

☐ Estimated OTH/HF Radar Range

Radar buffers drawn from precise tower locations. Radar Horizon Ranges calculated assuming 0m altitude for "Surface"; 3000m altitude for "Mid"; and 10000m altitude for "High". Each range calculated per individual tower height. Weapon system buffers drawn from island centroids based on data found in Table 1.

Service Layer Credits: Esri, HERE, DeLorme, MapmyIndia, © OpenStreetMap contributors, and the GIS user community. Satellite Image(s) Courtesy of the DigitalGlobe Foundation.

HQ-9 SAM Range

Radar buffers drawn from precise tower locations. Radar Horizon Ranges calculated assuming 0m altitude for "Surface"; 3000m altitude for "Mid"; and 10000m altitude for "High". Each range calculated per individual tower height. Weapon system buffers drawn from island centroids based on data found in Table 1.

Service Layer Credits: Esri, HERE, DeLorme, MapmyIndia, © OpenStreetMap contributors, and the GIS user community. Satellite Image(s) Courtesy of the DigitalGlobe Foundation.

Appendix D: Equations & Syntaxes

Equation 1

$$D_h \approx \sqrt{2 \cdot R \cdot H}$$

Equation 2

$$D_h \approx 3.57 \cdot \sqrt{H}$$

Equation 3

$$D_h \approx 4.12 \cdot \sqrt{H}$$

Equation 4

$$D_{max} \approx 4.12 \cdot \left(\sqrt{H_{Origin}} + \sqrt{H_{Target}} \right)$$

Equation 5

$$H_{Unknown} \approx \left(\frac{D_{max}}{4.12} - \sqrt{H_{Known}} \right)^2$$

Equation 6

$$x \tan \theta = h$$

Syntax 7

[Photogrammetric Height] = [Shadow Length]*TAN(RADIANS ([Solar Altitude]))

Syntax 8

[Range] = 4.12*((SQRT([Absolute Height])+SQRT([Investigated Altitude])))*1000

Syntax 9

[Unknown Height] = ((([Range]/4.12)-(SQRT([Known Height])))^2